EFFECT OF NANOCELLULOSE REINFORCEMENT ON THE PROPERTIES OF POLYMER COMPOSITES

by

Shikha Shrestha

A Dissertation

Submitted to the Faculty of Purdue University

In Partial Fulfillment of the Requirements for the degree of

Doctor of Philosophy

School of Materials Engineering

West Lafayette, Indiana

May 2019

THE PURDUE UNIVERSITY GRADUATE SCHOOL
STATEMENT OF COMMITTEE APPROVAL

Dr. Jeffrey P. Youngblood, Chair
School of Materials Engineering
Dr. Carlos J. Martinez
School of Materials Engineering
Dr. David Johnson
School of Materials Engineering
Dr. John Howarter
School of Materials Engineering

Approved by:
Dr. David Bahr
Head of the Graduate Program

To Mom, Dad and Dada

ACKNOWLEDGMENTS

I would like to express my sincere gratitude to my advisor, Professor Jeffrey Youngblood, for his constant support, assistance, and expertise throughout my research. His encouragement for me to venture into new research on my own and to pursue professional development during the last two years meant a great deal to me. I would like to thank my committee members, Professor Carlos Martinez, Professor John Howarter, and Professor David Johnson for their valuable time and feedback, which steered my research into right direction. I would also like to thank Dr. Gregory T. Schueneman at the USDA Forest Products Laboratory and Dr. James F. Snyder at the U.S. Army Research Laboratory, for their expertise and constant experimental support.

This work would not have been possible without the help of Dr. Shane Peng, Dr. Jairo A. Diaz, Dr. Youngman Yoo, Dr. Francisco Montes, Reaz Chowdhury, Kit Valone, Siavash Ghanbari, Mike Toomey, and all my group members.

I am also very thankful to my undergraduate advisor, Professor Richard Sisson for encouraging me to pursue Ph.D., and my mentor and a good friend, Abhishek Patnaik for his continuous support and valuable career advice.

Lastly, I would like to thank my parents for their endless love and care; my brother Kaushal, who is my role model and guardian, for providing me with constant support and encouragement in whatever I do; and to Ravi, for always being there for me.

This work has been supported by Private-Public Partnership for Nanotechnology in the Forestry Sector (P3Nano) under Grant No. 107528, and the Purdue Graduate School via Frederick N. Andrews Fellowship.

TABLE OF CONTENTS

LIST OF TABLES

LIST OF FIGURES

ABSTRACT

Author: Shrestha, Shikha. PhD
Institution: Purdue University
Degree Received: May 2019
Title: Effect of Nanocellulose Reinforcement on the Properties of Polymer Composites
Committee Chair: Jeffery Youngblood

Polymer nanocomposites are envisioned for use in many advanced applications, such as structural industries, aerospace, automotive technology and electronic materials, due to the improved properties like mechanical strengthening, thermal and chemical stability, easy bulk processing, and/or light-weight instigated by the filler-matrix combination compared to the neat matrix. In recent years, due to increasing environmental concerns, many industries are inclining towards developing sustainable and renewable polymer nanocomposites. Cellulose nanomaterials (CNs), including cellulose nanocrystals (CNCs) and cellulose nanofibrils (CNFs), have gained popularity due to their excellent mechanical properties and eco-friendliness (extracted from trees, algae, plants etc.). However, to develop CN-reinforced nanocomposites with industrial applications it is necessary to understand impact of hygroscopic swelling (which has very limited quantitative study at present), aspect ratio, orientation, and content of CNs on the overall performance of nanocomposites; and overcome the low dispersibility of CNs and improve their compatibility with hydrophobic matrix. In this work, we attempt to understand the influence of single nanocrystals in the hygroscopic and optical response exhibited by nanostructured films; effect of CNCs on the properties of PVA/CNC fibers by experimental evidence with mathematical modeling predictions; and hydrophobized CNFs using a facile, aqueous surface modification to improve interfacial compatibility with epoxy.

To evaluate the effect of CNC alignment in the bulk response to hygroscopic expansion, self-organized and shear-oriented CNC films were prepared under two different mechanisms. The coefficient of hygroscopic swelling (CHS) of these films was determined by using a new contact-free method of Contrast Enhanced Microscopy Digital Image Correlation (CEMDIC) that enabled the characterization of dimensional changes induced by hygroscopic swelling of the films. This method can be readily used for other soft materials to accurately measure hygroscopic strain in a non-destructive way. By calculating the CHS values of CNC films, it was determined that hygroscopic swelling is highly dependent on the alignment of nanocrystals within the films, with aligned CNC films showing dramatically reduced hygroscopic expansion than randomly oriented films. Finite element analysis was used to simulate moisture sorption and kinetics profile which further predicted moisture diffusion as the predominant mechanism for swelling of CNC films.

To study the effects of different types and aspect ratios of CNCs on mechanical, thermal and morphological properties of polyvinyl alcohol (PVA) composite fibers, CNCs extracted from wood pulp and cotton were reinforced into PVA to produce fibers by dry-jet-wet spinning. The fibers were collected as-spun and with first stage drawing up to draw ratio 2. The elastic modulus and tensile strength of the fibers improved with increasing CNC content (5 – 15 wt. %) at the expense of their strain-to-failure. The mechanical properties of fibers with cotton CNC were higher than the fibers with wood CNC when the same amount of CNCs were added due to their higher aspect ratio. The degree of orientation along the spun fiber axis was quantified by 2D X-ray diffraction. As expected, the CNC orientation correlates to the mechanical properties of the composite fibers. Micromechanical models were used to predict the fiber performance and compare with

experimental results. Finally, surface and cross-sectional morphologies of fibers were analyzed by scanning electron microscopy and optical microscopy.

To improve the dispersibility and compatibility of CNFs with epoxy, CNFs were modified by using a two-step water-based method where tannic acid (TA) acts as a primer with CNF suspension and reacts with hexadecylamine (HDA), forming the modified product as CNF-TA-HDA. The modified (-m) and unmodified (-um) CNFs were filled into hydrophobic epoxy resin with a co-solvent (acetone), which was subsequently removed to form a solvent-free two component epoxy system, followed by addition of hardener to cure the resin. Better dispersion and stronger adhesion between fillers and epoxy were obtained for m-CNF than the um-CNF, resulting in better mechanical properties of nanocomposites at the same loading. Thermal stability and the degradation temperature of m-CNF/epoxy improved when compared to neat epoxy.

CHAPTER 1. INTRODUCTION

1.1 Background and Motivation

Polymer nanocomposites have been a subject of interest due to their significantly improved mechanical performance, thermal stability, and barrier properties when compared to neat polymer or conventional composites even at low filler content. At present, many polymer nanocomposites are commonly incorporated with synthetic fillers like glass[1] and carbon[2,3] which are extensively used in advanced engineering applications, such as aerospace, automotive, packaging, and construction due to their unique combinations of high strength and stiffness with low density.[4–6] However, there are some drawbacks of these fillers such as high cost and energy consumption during production, difficulty in recycling, and potential health hazards posed by these inorganic fillers.[5,7] Therefore, due to increasing concern for environmental conservation, there has been extensive interest in biopolymer-based, renewable and sustainable natural fiber-based composites. Some of the key advantages of natural fiber-based composites over petroleum-based polymer and traditional composites are reductions in weight and cost, eco-friendliness, and recyclability.[7,8] A few examples of natural fibers used in composite applications are kenaf, hemp, flax, jute, and sisal.[9,10] However, natural fibers lack good mechanical properties in comparison with conventional reinforcing fillers such as a glass and carbon fibers.

In recent years, cellulose nanomaterials have emerged as a promising candidate for sustainable polymer reinforcement in nanocomposites. Cellulose is the most abundant natural resource on earth and can be extracted from various sources such as trees, plants, bacteria, algae, and tunicates[8,11–13]. They consist of a linear chain polysaccharide with repeated β-(1→4)-D-glucopyranose units, as shown in Figure 1.1. Cellulose nanocrystals

(CNCs) and cellulose nanofibrils (CNFs) are two classes of cellulose nanomaterials with superior mechanical properties and have abundant hydroxyl groups on their surfaces forming hydrogen bonds and allowing potential surface modifications[8,11]. Both CNCs and CNFs are chemically similar but have dissimilar physical characteristics as they have different colloidal forms. Transmission electron microscopy (TEM) images of CNCs and CNFs are shown in Figure 1.2.

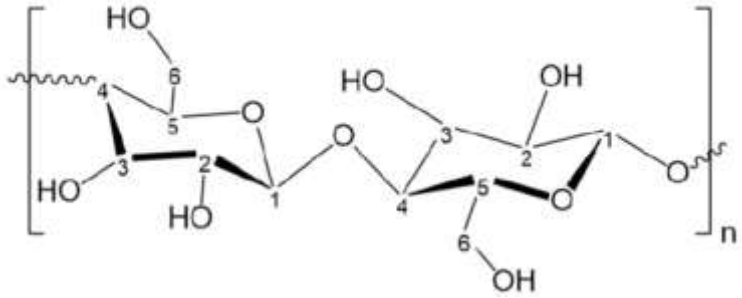

Figure 1.1 Repeating unit of Cellulose

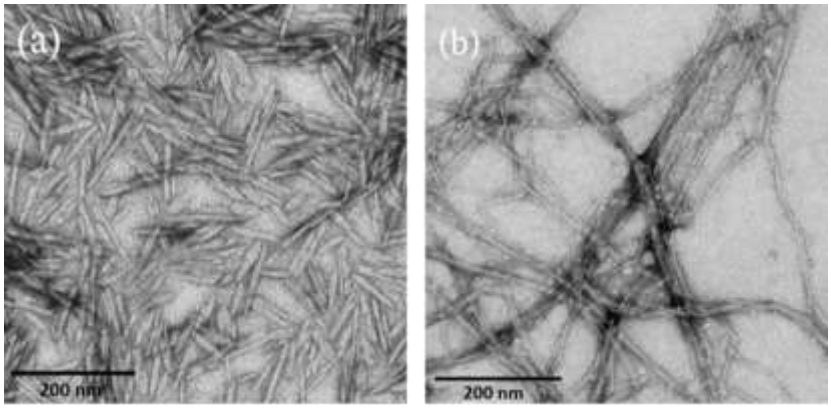

Figure 1.2 Transmission Electron Microscopy images of (a) CNC and (b) CNF

CNCs are rod-like or whisker shaped crystal structures with dimensions of 3 – 10 nm in width and 50 – 500 nm in length[14,15] and are extracted by controlled acid hydrolysis of cellulose-based materials. Acid treatments remove most of the amorphous regions from the cellulose and leave behind highly crystalline CNCs. It has been reported that CNCs have axial elastic modulus (E_A = 110 – 220 GPa[16,17]) and tensile strength (estimated σ_f= 7.5 – 7.7 GPa[8]) higher than typical filler materials such as Kevlar, glass, and carbon fiber.[17] These excellent mechanical properties have led to incorporating CNCs as reinforcing agents into a wide range of thermoplastic and thermoset polymers, such as poly(vinyl alcohol)[18], poly(lactic acid)[19], polyethylene, starch, epoxy [20], and polyurethane [21]. CNFs are another cellulose-based nanomaterial with long flexible fiber network having dimensions of 4 – 20 nm width and > 1 μm length[22], but with higher aspect ratios than CNCs. The morphologies and dimensions of CNFs can vary significantly, depending on the degrees of fibrillation and types of pretreatment involved.[8,12] These nanofibrils can also be extracted from cellulose-based materials (e.g., wood pulp, cotton, hemp etc.) by mechanical grinding, high-shear homogenization or 2,2,6,6-tetramethylpiperidine-1-oxyl (TEMPO)-mediated oxidation[23–25]. CNFs exhibit both amorphous and crystalline cellulosic regions and possess large surface area with a web-like structure than CNCs, making them attractive fillers to achieve more effective reinforcement in polymer matrices.[26,27] Numerous studies using various CNFs have indicate that fibrils with smaller diameter and longer lengths exhibit stronger reinforcing effect.[28] These nanomaterials can also be used in applications such as organic electronics, fibers, cements, laminates, biomaterials, and packaging materials.[5,8,18,29]

Despite rapid expansion and moderate success of different applications of CNCs and CNFs, the effective polymer reinforcement has not been well understood due to cellulose nanomaterials' large variability.[8] In this work, we determine one of the important material properties i.e., coefficient of hygroscopic swelling of CNC films by using contact-free digital image correlation method. This property is very significant in variety of fields, such as pharmaceuticals[12,30] and electronic packaging,[31,32] where any swelling mismatch between polymers and moisture impermeable materials induces hygroscopic stresses leading to packaging failures.[31,32] Therefore, knowing this material property will be beneficial to avoid any failure in the CNC-based materials. Moreover, it is necessary to identify, control and understand how reinforcing CNCs lead to improvement in overall intrinsic properties of polymer nanocomposites. For this, PVA is used as an ideal matrix to fill CNCs because it is semi-crystalline, non-toxic, water soluble and have wide range of applications in tissue scaffolding,[33] filtration membranes, drug delivery[34] and optics.[35,36] Commercially, short-fibers of PVA are used as reinforcement in concrete.[37] Incorporating CNCs into PVA fibers results in improved mechanical properties of fibers yet maintaining eco-compatibility, and creation of light-weight and strong nanocomposites. It is easy to disperse and process cellulose nanomaterials in the hydrophilic matrices, however, the inherent incompatibility between the hydrophilic nanocellulose and the common hydrophobic polymer matrices remain a challenging issue during processing. Therefore, surface modification of native CNF/CNC has attracted much attention as a method to improve interfacial properties within the polymer matrix. Here, the hydroxyl groups of CNFs have been functionalized using a facile, aqueous and cost-effective method; it

increased the interfacial compatibility of CNFs and hydrophobic epoxy resin and improved dispersion, leading to high strength and stiff nanocomposite.

The research in this thesis are designed to motivate an integral understanding of processing-structure-property relationship of nanocellulose and nanocellulose reinforced polymer nanocomposites, leading the way to new possible applications for CNC/CNF-based materials.

1.2 Research Objectives

The goal of this work is to develop methods to disperse CNCs and CNFs in different hydrophilic and hydrophobic polymer matrices by improving the compatibility between filler-matrix and investigate their effects on the overall performance of nanocomposites. Several research objectives were established to achieve these goals, which are as follows:

1) Develop a metrology technique using a contact-free digital image correlation method to study an important material property i.e., hygroscopic swelling behavior in CNC films influenced by the CNC alignment. Compute mathematical model for hygroscopic expansion of CNC films as a function of water vapor sorption and study its kinetic behavior.
2) Develop industrially scalable process for CNC-nanocomposite fibers and investigate their mechanical and thermal properties influenced by different types and contents of CNCs. Compute the micromechanical models to predict the mechanical property improvement by accounting for CNC content, order parameter, and aspect ratio.
3) Improve the compatibility and dispersibility between CNFs and hydrophobic epoxy via water-based and cost-effective surface modification of CNFs. Investigate the

effects of modified CNFs on the mechanical, thermal and morphological properties of epoxy nanocomposites and compare the performance with the unmodified CNF and neat matrix.

1.3 Overview of this work

In this work, each chapter will describe one of the research objectives mentioned above. The literature background, research and results for each topic will be discussed separately in each chapter. Chapter 2 focuses on developing a metrology technique to determine an important material property i.e., CHS of CNC films as a function of CNC alignment. Contrast enhanced digital image correlation (CEMDIC) enabled the characterization of dimensional changes induced by the hygroscopic swelling of the films. The contact-free nature of this method isolated samples from mechanical or thermal interactions during hygroscopic swelling. The speckle patterns required for image correlations were obtained from characteristic structural domains of CNC films under polarized light. Additional insights into water intake of CNC films were obtained from moisture sorption isotherms measured via dynamic vapor sorption (DVS). Finite element analysis was also implemented to evaluate the dominant role of moisture diffusion in the sorption kinetic profiles. Chapter 3 focuses on using dry-jet-wet spinning as a technique to develop industrially scalable process for PVA/CNC composite fibers with high strength and modulus. CNCs hydrolyzed from wood and cotton (with different aspect ratios) were reinforced into PVA and spun into fibers, which was followed by first stage drawing. A systematic characterization of dispersion of CNCs in the PVA and its effects on mechanical and morphological properties of composite fibers is presented. Micromechanical models

are used to predict and compare the fiber performance. Chapter 4 presents processing and formulating a solvent-free mixture of epoxy resin and nanofibrils by reinforcing surface modified TEMPO-oxidized CNFs (TOCNF). This chapter explores modifying TOCNFs in a sustainable and cost-effective manner by altering their surface chemistry with a water-based method to improve the compatibility with the hydrophobic epoxy. A comparative study of thermal and mechanical properties of surface modified and unmodified CNFs reinforced into epoxy nanocomposites is discussed. The dispersibility study of CNFs is also presented.

CHAPTER 2. HYGROSCOPIC SWELLING DETERMINATION OF CELLULOSE NANOCRYSTAL FILMS BY POLARIZED LIGHT MICROSCOPY DIGITAL IMAGE CORRELATION

All lab- work was performed by Shikha Shrestha. All analysis except finite element analysis was performed by Shikha Shrestha with guidance of Dr. Jeffrey P. Youngblood. All writing was performed by Shikha Shrestha with guidance and editing by Dr. Jairo A. Diaz and Dr. Jeffrey P. Youngblood.

2.1 Introduction

CNCs have been used as substrates for electronics, semi-conductor layers, solar cells and as a filler in composites,[8,38–40] therefore, it is crucial to determine the CHS of CNC- based materials, and their corresponding mechanism for hygroscopic swelling.[41] CNCs are highly crystalline and in principle impenetrable by water,[42,43] however, when multiple CNCs stack to form nanostructured films, water molecules can freely diffuse throughout the film generating an average increase in CNC-CNC interspacing (i.e., CNC film swelling).[31,42–44] Thus, the distribution of CNC-CNC interfacial contacts (i.e., possible water adsorption sites)[43] throughout the film is expected to govern the resultant water intake. The role of CNC interfaces and CNC alignment in materials' properties has been explored before in the context of thermal conductivity.[45]

Hygroscopic swelling, or expansion of a material, is commonly characterized by the CHS, which correlates the degree of expansion of a material to the mass intake of water as a function of humidity. CHS values are crucial in fields like pharmaceuticals, where the interaction of water with cellulosic material is critical for formulation, processing and product performance.[12,30,46] In electronic packaging,[32] some polymeric materials can absorb moisture and swell, whereas the adjacent materials (e.g., lead frame, die paddle, and silicon chip, etc.) are typically impermeable to moisture. This swelling mismatch between different materials induces hygroscopic stress that leads to package failures.[32,47] Therefore, it is important to determine the CHS values of CNCs in order to avoid these failures.

Measurement of hygroscopic swelling of polymer films has been conducted by various experimental techniques such as Michelson interferometry, Moiré interferometry, and the Archimedian method.[48–50] However, the estimation of dimensional changes is difficult for CNC- based materials due to the plasticizing effect of water that leads to low strength of swelled films.[13] Quartz crystal microbalance with dissipation monitoring (QCM-D) and spectroscopic ellipsometry (SE), have also been used to measure water vapor intake, swelling thickness, dynamic modulus dissipation and has been used for CNC films before.[42,50] Nonetheless, the excessive preparation time required for highly accurate samples can affect the estimation of the instantaneous swelling.[42,51,52]

Here, we use CEMDIC[53] to determine CHS of CNC films as a function of CNC alignment. The contact-free nature of CEMDIC isolated CNC films from mechanical or thermal interactions during hygroscopic swelling. Likewise, speckle patterns required for image correlations were obtained from characteristic structural domains of CNC films under polarized light. Additional insights into water intake of CNC films were obtained

from moisture sorption isotherms measured via dynamic vapor sorption (DVS). We finally intent to capture the moisture sorption and kinetic profiles of CNC films by fitting to conventional models used in cellulosic materials. First, we used the Guggenheim, Anderson, and deBoer (GAB) model[54–56] to capture moisture sorption profiles due to its ability to represent sigmoidal shaped isotherms. Second, moisture kinetic profiles were captured with parallel exponential kinetics, PEK model,[57,58] as sorption kinetic profiles can be deconvoluted into fast and slow exponential processes that connect characteristic times and moisture contents. A complementary finite element analysis (FEA) seeks to evaluate the dominant role of moisture diffusion in the kinetic profiles.

2.2 Materials

Water suspensions of 11.8 wt.% cellulose nanocrystals (batch # 2014-FPL-CNC-064: 1 wt.% sulfur content in sulfate half-ester form and sodium as counter ion) were produced at the USDA Forest Service-Forest Products Laboratory (FPL), Madison, WI.[59]

2.3 Method

2.3.1 CNC Film Preparation and CNC Alignment Characterization

Self-organized and shear-oriented CNC films were prepared in a method similar to that of Diaz et al.[41] For self-organized films, an aqueous 1.6 wt.% CNC suspension was poured into polystyrene petri dishes (d: ~ 8 cm) as shown in Figure 2.1(a) and allowed to evaporate under ambient conditions (23^{o}C, 35% relative humidity) for three-five days.[41,60] For shear-oriented films, 3 mL of 11.8 wt.% CNC suspensions were cast on a glass substrate between two 0.6 mm thick polyethylene terephthalate (PET) strips. High CNC concentration was used to effectively induce CNC alignment during shearing and retain it

during film formation.[60] A regular 4 cm wide razor blade was vertically inclined to 45° with respect to the substrate to shear the films as shown in Figure 2.1(b). This process was repeated for six passes. After shear casting, all films were allowed to evaporate for three days under ambient conditions.[41,60] Dry self-organized and shear-oriented CNC films were peeled off from the substrate and cut into test specimens of ~ 35 µm × 20 mm × 5 mm using a razor blade.

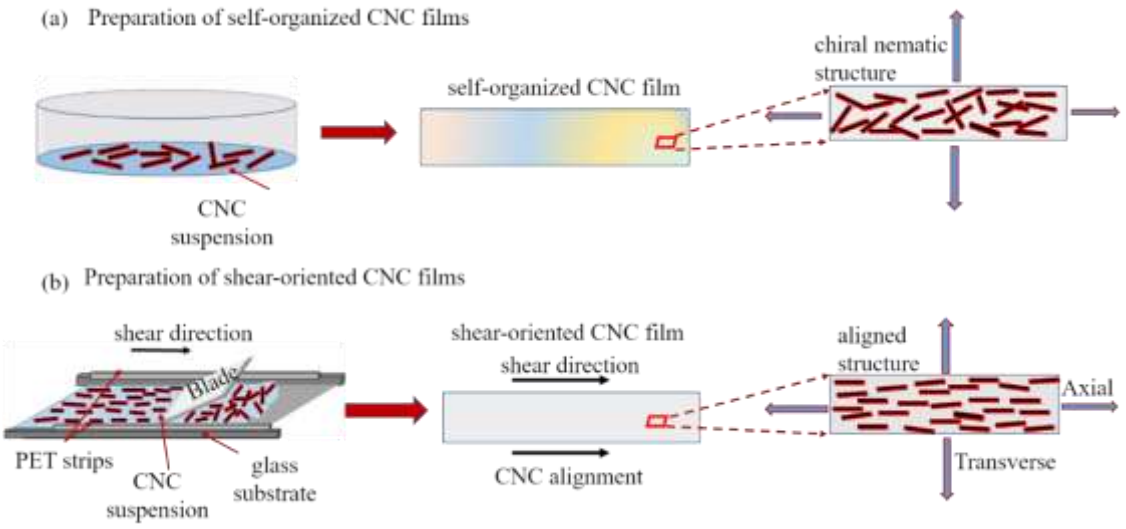

Figure 2.1 Schematic of preparation of the CNC films by casting method for (a) self-organized and (b) shear-oriented films. The directionality of the shear cast films was defined as "axial" or "transverse" for the direction parallel to or perpendicular to the shear direction.

CNC alignment within the films was evaluated in a Bruker GADDS 2D X-ray diffractometer (2D-XRD) using a source of 546 nm Cuα at 40 mA, 20 kV for 360 s and a beam diameter of 500 µm at 6.1 cm from the detector in transmission mode. Herman's order parameter (S) was calculated in order to estimate the in-plane CNC alignment through the entire film thickness where, $S = 0.0$ and $S = 1.0$ represented no preferential orientation and a fully aligned film, respectively. The integration of intensity (I) versus

azimuthal angle (ϕ) was performed from 0° to 180° around (200) crystal plane present at 2θ: {21.0 – 22.3} for cellulose Iβ, after subtracting the background and the equations are:

$$S = \frac{3\langle cos^2\gamma\rangle - 1}{2} \tag{2.1}$$

$$\langle cos^2\gamma\rangle = 1 - 2\langle cos^2\phi\rangle \tag{2.2}$$

$$\langle cos^2\phi\rangle = \frac{\int I(\phi)cos^2\phi\ sin\phi\ d\phi}{\int I(\phi)sin\phi\ d\phi} \tag{2.3}$$

2.3.2 Hygroscopic Swelling Determination in CNC films

CNC films were introduced into a sealed glass chamber (7.5 cm × 5 cm × 2.5 cm), where water vapor (ultrasound humidifier) and dry nitrogen were flown at a rate of ~ 0.15 m^3/h at room temperature. The flow mixture was equilibrated for five to eight minutes, until as stable relative humidity (RH) value was obtained. RH was measured adjacent to the sample using a USB Temperature and Humidity sensor (USB-TRH200) and QTenki data logger software. The humidity chamber was connected to the exit valve to vent the chamber after the experiment.

Digital Image Correlation (DIC) was used to measure the hygroscopic strains of CNC films in a manner similar to Diaz et al.[41] Contact-free optical measurements with full-field displacements of the films were computed using images of the specimen at the initial and deformed stages.[53,61,62] Images of CNC films were taken using a Carl Zeiss (Axio Observer A1) inverted microscope in transmission mode. Speckle patterns were generated

between crossed polarizers using 5× magnification. Five different contact-free images of 36 bit and 2047 × 2047 pixels, were captured at RH of 0, 10, 20, 30, 40, 50, 60, 70, 80, 90 and ~ 97%. The images were processed using ImageJ and Adobe Photoshop to adjust different properties such as bit transformation, rotations, image contrast, etc. and obtain distinct speckle patterns. Images were correlated with MatLab 8.2 image toolbox (cpcorr.m) together with the (HighCorr package) designed by R J. Thompson et al.[63]

2.3.3 Dynamic Vapor Sorption Analysis of CNC Films

Water vapor intake of CNC films was measured using TA instruments Q5000 Dynamic Vapor Sorption Analyzer at 23°C. Moisture adsorption and desorption isotherms for self-organized and shear-oriented CNC films were generated by varying RH (10% increments), starting from 0 to 97.5% while recording cumulative film weight. Equilibrium was assumed when there was no more than 1 μg of change in film weight over a period of 15 minutes. The mass change was constantly monitored as a function of time during ~ 12.5 days.

2.3.4 Modeling and Simulation

A transient finite element method was implemented to assess water vapor intake into CNC films and complement experimental evidence for moisture sorption kinetic profile. The specific goals of the FEA modeling are: (i) to determine if the films are thin enough for assumption of equilibrium and uniform water content in the film at the time of measurement, and (ii) to test whether capillarity affects water intake. This was done by simulating moisture diffusion into the CNC films at different RH. Film geometry was considered a rectangle of dimensions 20 mm × 5 mm, accommodated in one asymmetric modeling space using an ABAQUS 6.14. The model was meshed by 4-node linear

axisymmetric heat transfer quadrilateral elements. During simulation, diffusion coefficients for different RH were obtained from literature.[64]

During water vapor diffusion at constant temperature for CNC films, it is assumed that the process follows Fick's second law[65], which is given by

$$\frac{\partial C}{\partial t} = \nabla.(D\nabla C) \tag{2.4}$$

where, C is the moisture content in the film at a specified time t and D is the diffusion coefficient. This equation can be simplified as

$$\frac{\partial C}{\partial t} = D(\frac{\partial^2 C}{\partial x^2} + \frac{\partial^2 C}{\partial y^2} + \frac{\partial^2 C}{\partial z^2}) \tag{2.5}$$

Furthermore, it can be written in terms of percentage moisture content[66], which is given by

$$\frac{\partial C}{\partial t} = D(\frac{\partial^2 m}{\partial x^2} + \frac{\partial^2 m}{\partial y^2} + \frac{\partial^2 m}{\partial z^2}) \tag{2.6}$$

In order to obtain the flux of water (J) in the CNC film, the FEA method was applied to the following equation[67]

$$J = -D.\left[S\frac{\partial \emptyset}{\partial x} + \emptyset\frac{\partial S}{\partial x}\right] \tag{2.7}$$

where, S is the solubility of water, $\emptyset$ is the activity of the diffusion material which is equal to C/S, and C is the mass content for material diffusion. Crank-Nicholson, a highly

accurate finite difference method which is unconditionally stable for diffusion equations, was used to solve for transient diffusion analysis.[64] The moisture diffusion was considered in one dimension and boundary conditions were applied, where the initial RH was set to zero and the films were humidified to the saturated moisture content for 15 hours. Different RH values were considered for varying boundary conditions, which led to the calculation of time-dependent water vapor solute atoms by simulation.

2.4 RESULTS AND DISCUSSION

2.4.1 Hygroscopic Strain and Swelling in CNC films

Self-organized films ($S \sim 0.04$) exhibited the typical iridescent optical response associated to the constructive light interference generated by chiral nematic domains within the film (Figure 2.2(a)). As CNCs align, such a structural coloration is effectively removed as observed for highly transparent shear-oriented films ($S \sim 0.8$) with little light interference (Figure 2.2(b)). Likewise, water absorption can affect the CNC film coloration by inducing structural changes (Figure 2.3(a) – (c)). CNC-CNC interspacing can be effectively increased as water penetrates and adsorbs throughout the films.[68] Water molecules can adsorb in two distinct ways in polymeric materials: (i) by free and adsorbed molecules filling in voids, which can easily move through the free volume,[69] and (ii) by disrupting polymers inter-chain via hydrogen bonding.[69–71] In CNC films, water cannot enter individual crystals, hence, the only possible ways of water adsorption are by diffusion of water molecules through the voids between the crystals and adsorption at either their surfaces or at the interfaces between CNCs.[42] Of the two, only interfacial adsorption causes film expansion as the water acts to drive crystals apart. As water vapor intake increases,

water condensation can occur, which can trigger nanocrystals reorientation and irreversible film hydration.[42,44]

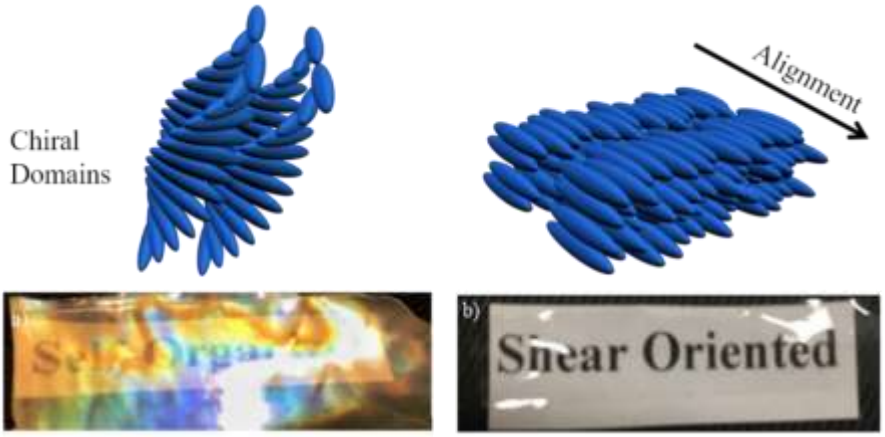

Figure 2.2 (a) Iridescent self-organized CNC film with chiral nematic domains (b) transparent shear-oriented CNC film with aligned structure.

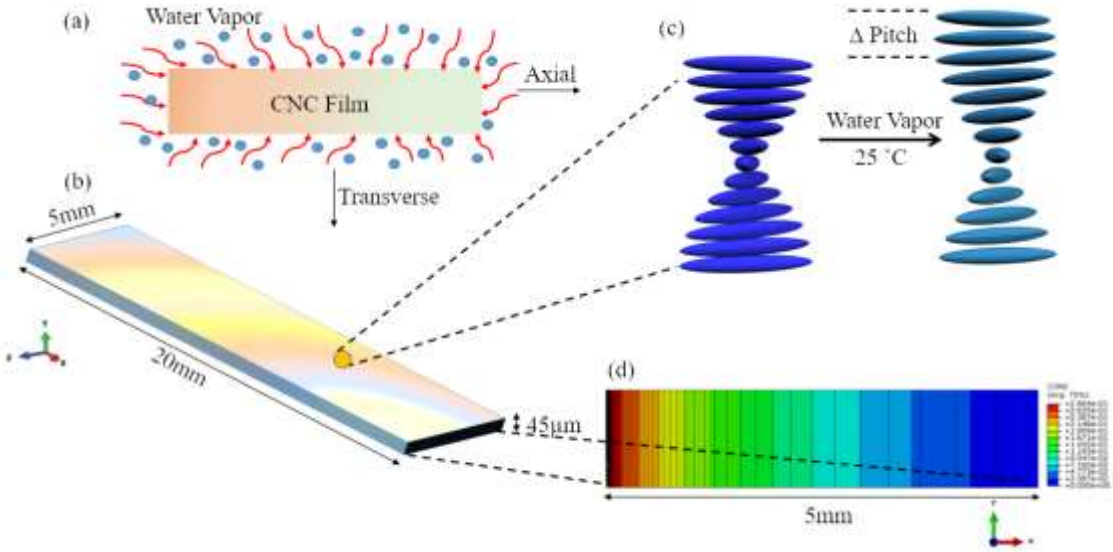

Figure 2.3 Deformation behaviors of a CNC film through moisture sorption. (a) a schematic of the moisture diffusion into the CNC film, (b) 3D schematic of the CNC film for moisture diffusion analysis, (c) increasing interspaces between the CNCs as water diffuses into the films and (d) contour of simulation of moisture diffusion after 15 hours.

Hygroscopic strains were obtained by correlating the cross-polarized microscopy images of CNC films as a function of RH (Figure 2.4). The extent of swelling for both self-organized and shear-oriented films was smaller at lower RH. For instance, as RH increases from 10 to 50 %, variations of hygroscopic strain ($\Delta\varepsilon$) of ~ 0.007 %strain/%C were recorded. Shear-oriented films exhibited similar reduced expansion in the direction parallel ($\Delta\varepsilon_{\parallel}$ ~ 0.051 %strain/%C) and perpendicular to CNC alignment ($\Delta\varepsilon_{\perp}$ ~ 0.420 %strain/%C). This may be associated to adsorbed water vapor filling in the voids between the crystals, causing no significant change in thickness, and thus no swelling of the films.[72] In contrast, the swelling increased significantly at higher RH. For RH values from 60 to 97%, $\Delta\varepsilon$ ~ 1.00 %strain/%C, (self-organized) and $\Delta\varepsilon_{\parallel}$ = 0.5 %strain/%C, $\Delta\varepsilon_{\perp}$= 4.02 %strain/%C, (shear-oriented). At high RH, water molecules can effectively penetrate between the crystals, causing an overall increase in thickness and ultimately swelling of the films. Niinivaara et al.,[42] and Aulin et al.,[44] also observed changes in film thickness with increasing RH. The in-plane hygroscopic expansion of self-organized films was isotropically increased in all directions. Due to CNC alignment in shear-oriented films, the hygroscopic response was clearly anisotropic, where expansion was significantly larger in the transverse (perpendicular) than in the axial (parallel) direction to the shear alignment (i.e., $\varepsilon_{\perp} > \varepsilon_{\parallel}$). Overall structural differences between shear-oriented and self-organized films can influence water vapor penetration throughout the film. For instance, alignment of crystals in shear-oriented CNC films results in better nanocrystal packing (ρ ~ 1.55 g/cm^3) than in self-organized films (ρ ~ 1.45 g/cm^3), suggesting a more tortuous transport of water molecules in specific directions as alignment increases in CNC films. As well, it

is logical that the higher density coupled with alignment leads to more interfaces between CNCs in the transverse direction due to better packing, leading to higher hygroscopic strain with humidity in that direction, which is in fact, observed.

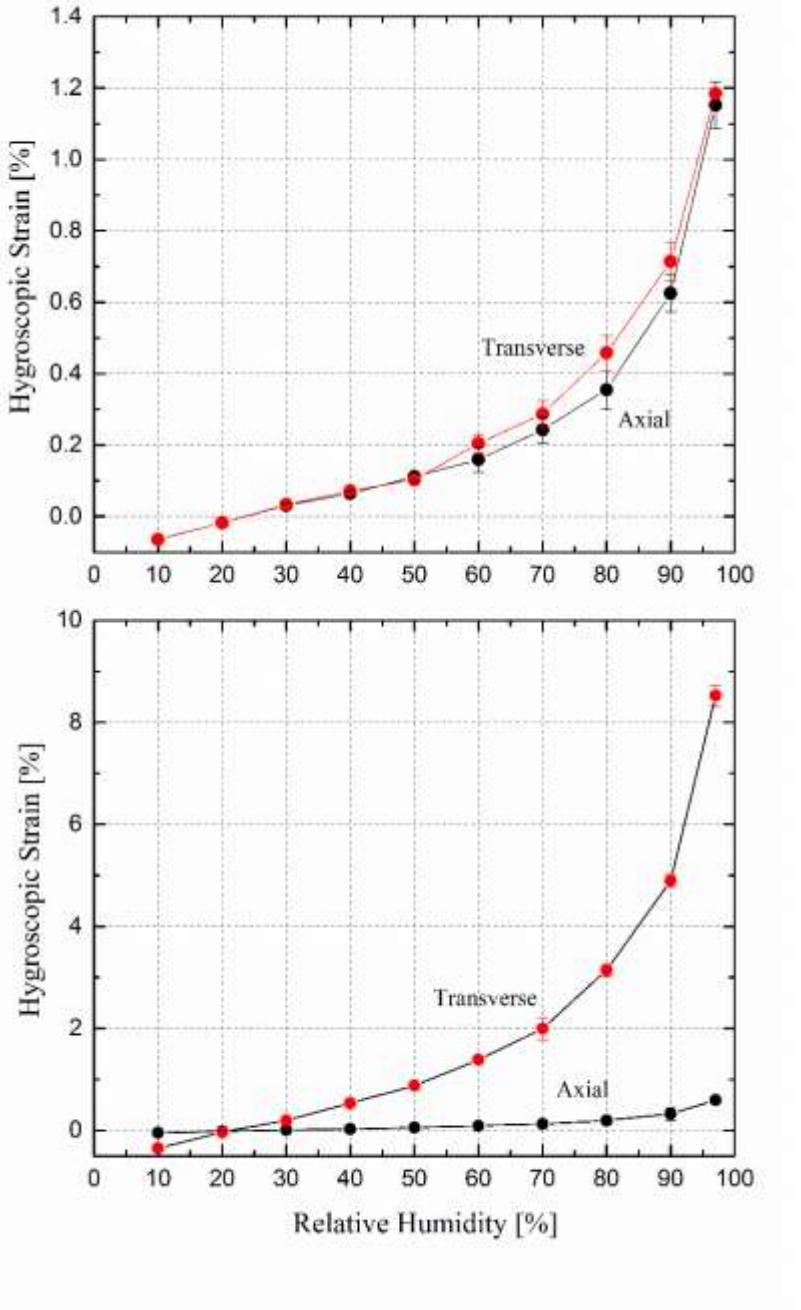

Figure 2.4 Hygroscopic strain as a function RH for CNC films (a) self-organized and (b) shear-oriented CNC films for axial (—•—) and transverse (—•—) directions.

2.4.2 Water Vapor Adsorption and Desorption Isotherm Analysis

The experimentally measured moisture adsorption-desorption isotherms for self-organized and shear-oriented CNC films are shown in Figure 2.5(a) and Figure 2.5(b), respectively. Water adsorption on CNC films occurs as water penetrates through voids between crystals. But this might not happen during desorption due to large number of hydroxyl groups compared to adsorption (i.e., high hydrogen binding strength generated during adsorption).[42,73–75] The sorption isotherms for CNC were characterized by a type II sigmoidal shaped profile as seen in the plots. The hysteresis observed is a typical phenomenon in sorption isotherms of cellulose-based materials and can be generalized to many hydrophilic materials.[76–80] Some of the previously reported explanations for this hysteresis are increase in the strength of solid-liquid bonding (enthalpy effect), ordering of molecules (entropy effect), change in chain configuration (irreversible swelling or chain relaxation), or by the entry of water into the film structure.[54,79,81] Since they were cast from the same aqueous suspension of CNC, both self-organized and shear-oriented films have the same chemical structure and properties. Hence, both the films absorbed approximately the same amount of water, as shown in Figure 2.5.

The GAB model has been successfully applied for predicting moisture sorption properties of cellulosic materials.[77] This model explains the adsorption of an intermediate state of vapor between the monolayer water and the condensed molecules adsorbed at higher RH. Water molecules in the intermediate state are considered to interact with the CNC where there is a concentrated hygroscopic response at the interface; however, the interaction is weak compared to the CNC and monolayer interaction.[77] The simple GAB equation is given by:

$$W = \frac{W_m \, C_G K (\frac{P}{P_o})}{\left[1 - K\left(\frac{P}{P_o}\right)\right]\left[1 - K\left(\frac{P}{P_o}\right) + C_G K\left(\frac{P}{P_o}\right)\right]} \tag{2.8}$$

where, W represents the grams of water sorbed per gram of solid i.e., CNC film, W_m represents the grams of water in the form of a monolayer. C_G and K are parameters related to the heat of sorption of the monolayer and intermediate layer, respectively and $(\frac{P}{P_o})$ is the water vapor relative pressure. Temperature effects were incorporated into the GAB equation using the Arrhenius equation by relating a reaction constant (C_o, K_o) with the activation energy $(\Delta \mathrm{H}_c, \Delta \mathrm{H}_K)$

$$C_G = C_o \exp\left(\frac{\Delta \mathrm{H}_c}{RT}\right) \tag{2.9}$$

$$K = K_o \exp\left(\frac{\Delta \mathrm{H}_K}{RT}\right) \tag{2.10}$$

$T =$ absolute temperature (K) and $R =$ universal gas constant $(8.314 \ \mathrm{J/mol/K})$. [55]

Equation (2.8) was fitted to the moisture sorption data of CNCs by direct non-linear regression analysis[82] and the parameters are presented in Table 2.1. Figure 2.5 shows a good fit of the GAB equation to the experimental data.

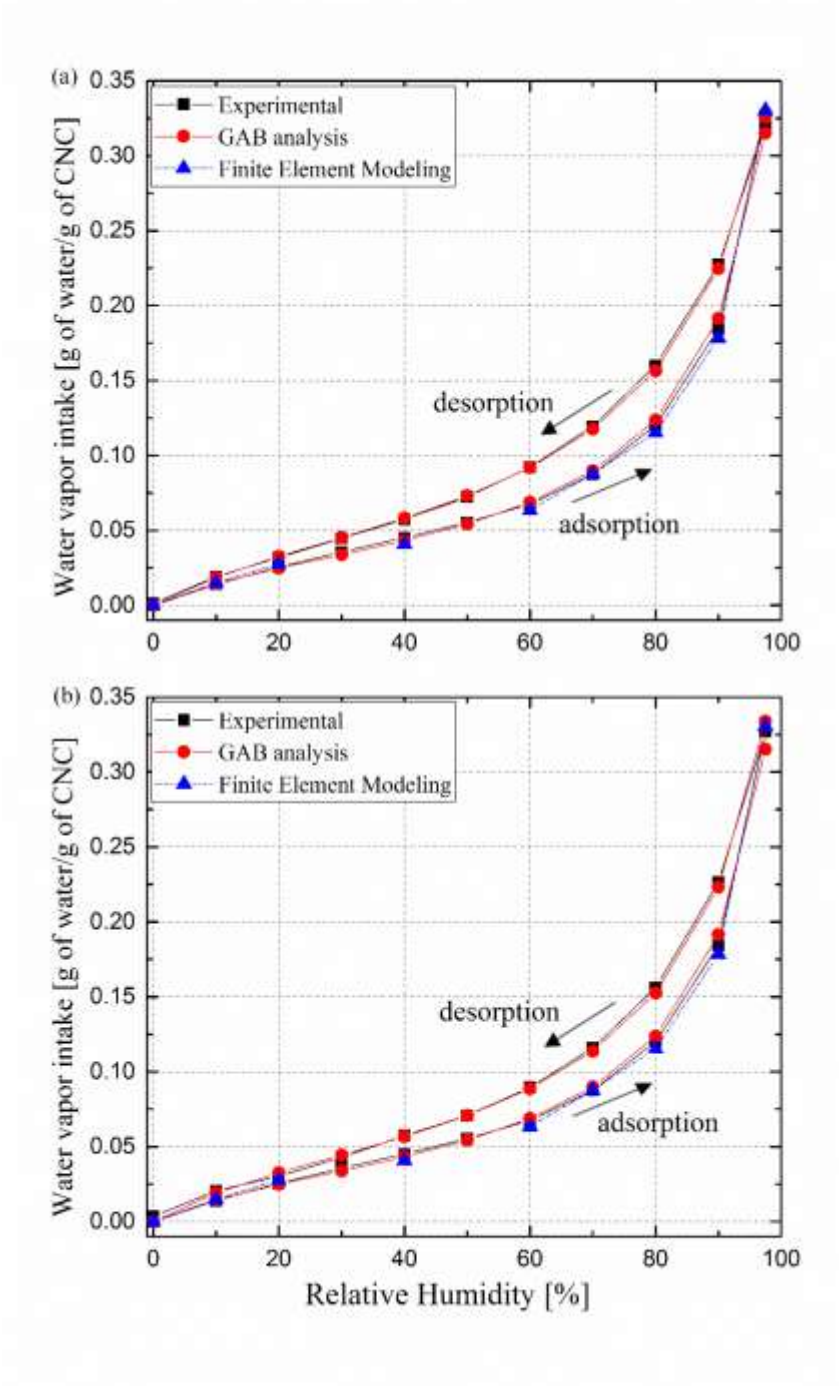

Figure 2.5 Moisture adsorption-desorption profile of CNC film (a) self-organized (b) shear-oriented at 23°C exhibiting experimental, GAB analysis and Finite Element Analysis model.

The monolayer coverage by water (value of W_m from the GAB equation) was slightly higher during desorption than for adsorption (Figure 2.5 and Table 2.1). This is due to greater availability of primary sites at higher RH.[79] Furthermore, Zografi et al. [79] extended the GAB analysis to account for water intake by non-crystalline or disordered regions of cellulose. They proposed a correction factor W_m^{Corr}, given by the ratio of W_m to the fraction of the non-crystalline region in the cellulose.[76] For the CNC films used in this work, the pure crystalline region was determined to be 72%[83] (~ 28% associated with surface disordered regions remaining after acid hydrolysis). Hence, W_m^{Corr} was calculated by assuming the fraction of disordered region to be 28%. Both values of W_m and W_m^{Corr} for the two films were identical, indicating no significant difference in their ability to bind water molecules for monolayer coverage. Studies have shown that the degree of crystallinity and chemical affinity play a vital role when comparing W_m and W_m^{Corr} of other cellulosic materials as seen in Table 2.2. As expected, types of cellulose with different degrees of crystallinity exhibit different values of W_m. However, after correcting for the degree of crystallinity, all values were in reasonable agreement with each other and with the W_m^{Corr} obtained from the CNC films presented in this study. For all types of cellulose, adsorption was approximately 0.102 ± 0.1708 g of water per g of cellulose, which is similar to the values obtained for CNC films in this study (Tables 2.1 and 2.2). The relative ability to bind water molecules for monolayer coverage between CNC and other cellulosic materials might be connected to the high degree of overall crystallinity present in CNC films.

Table 2.1 Computed values of GAB parameters and correlation coefficients obtained from analysis of moisture sorption isotherms of CNC films.

CNC Films		Crystallinity (%)	W_m (g/g)	W_m^{Corr} (g/g)	C_G	K	Ref.
self-organized	adsorption	72[83]	0.033	0.124	6.518	0.912	this work
	desorption		0.052	0.186	5.129	0.867	
shear-oriented	adsorption	72[83]	0.035	0.125	6.004	0.913	
	desorption		0.048	0.172	5.896	0.882	

Table 2.2 Amount of water sorbed by various celluloses at the monolayer corrected for degree of crystallinity[79].

Sample	Crystallinity (%)	W_m (g/g)	W_m^{Corr} (g/g)	Ref.
Cotton	70	0.032	0.107	[84]
Cellophane	70	0.059	0.098	[30]
Microcrystalline Cellulose	63	0.036	0.096	[75]
Microcrystalline Cellulose	40	0.066	0.107	[84]

2.4.3 Water Vapor Adsorption and Desorption Kinetics Analysis

Moisture gain and loss of the CNC films during the sorption experiments were gravimetrically measured using DVS. Kinetically, the mechanisms of moisture sorption in such hydrophilic materials are complex because of the continuously changing structure of the films due to swelling.[85] Moreover, the adsorption-desorption kinetics on each level of relative humidity can be modelled by two parallel independent first order processes taking place simultaneously (PEK model). The model offers fast and slow mechanisms for the exchange of water vapor at different sorption sites. It provides insight into the time scales

(rates) and the mass changes (extents) of the individual components. Here, the experimental data of the moisture content in self-organized and shear-oriented CNC films were fitted as a function of time. The general equations used for PEK's model are given by:

$$\text{Adsorption: } M_t = M_{1+2}(1 - e^{-t/(\tau_1+\tau_2)}) \quad (2.11)$$

$$\text{Desorption: } M_t = -M_{1+2}(1 - e^{-t/(\tau_1+\tau_2)}) \quad (2.12)$$

where, M_t is the mass change at any time t, M_1 and M_2 are the masses at equilibrium, τ_1 and τ_2 are characteristic times for which M_1 and M_2 are reached respectively, and M_{1+2} corresponds to the sum of M_1 and M_2. Subscripts 1 and 2 indicate a fast and a slow kinetic process, corresponding to the sorption sites.[86]

The predicted curves agreed with experimental data (R^2 ~ 0.999) for the self-organized and shear-oriented films, as shown in Figure 2.6, thus validating the PEK model as an appropriate model to describe the moisture sorption in CNC films. The PEK parameters M_1, M_2, τ_1 andτ_2 were calculated for lower RH (30%) and higher RH (90%) (Figure 2.6), and the values are listed in Table 2.3 and 2.4. It was observed that at the lower RH, the components of fast sorption were greater than that of the slow sorption process ($\tau_1 > \tau_2$ and $M_1 > M_2$).[85,86] At lower RH, water molecules can predominantly adsorb onto voids and nanopores, which would only lead to small structural changes. At higher RH, the components of slow sorption were dominant ($\tau_1 < \tau_2$ and $M_1 < M_2$). Since all adsorption sites were already occupied, the water molecules could only be adsorbed into the film by penetrating between the crystals. The adsorbed moisture induced distinct structural changes in the films, which contributed to the swelling. The PEK parameters for both types

of CNC films were found to be similar at the same RH value, as they were prepared from the same aqueous suspension of CNC.[85,86]

Table 2.3 Computed values of PEK's model parameters M_1, M_2, τ_1 and τ_2, corresponding to fast (1) and slow (2) kinetics for lower RH of 30%.

Relative Humidity 30%					
CNC Films	M_1	τ_1	M_2	τ_2	R^2
self-organized	0.782 ± 0.00128	59.7 ± 0.570	0.131 ± 0.00121	8.92 ± 0.0347	0.997
shear-oriented	0.825 ± 0.00324	60.97 ± 2.12	0.132 ± 0.00293	9.06 ± 0.0631	0.999

Table 2.4 Computed values of PEK's model parameters M_1, M_2, τ_1 and τ_2, corresponding to fast (1) and slow (2) kinetics for higher RH of 90%.

Relative Humidity 90%					
CNC Films	M_1	τ_1	M_2	τ_2	R^2
self-organized	0.972 ± 0.0061	14.8 ± 0.085	5.04 ± 0.0151	245.8 ± 3.34	0.999
shear-oriented	0.946 ± 0.0054	14.5 ± 0.061	5.31 ± 0.0177	240.7 ± 2.76	0.998

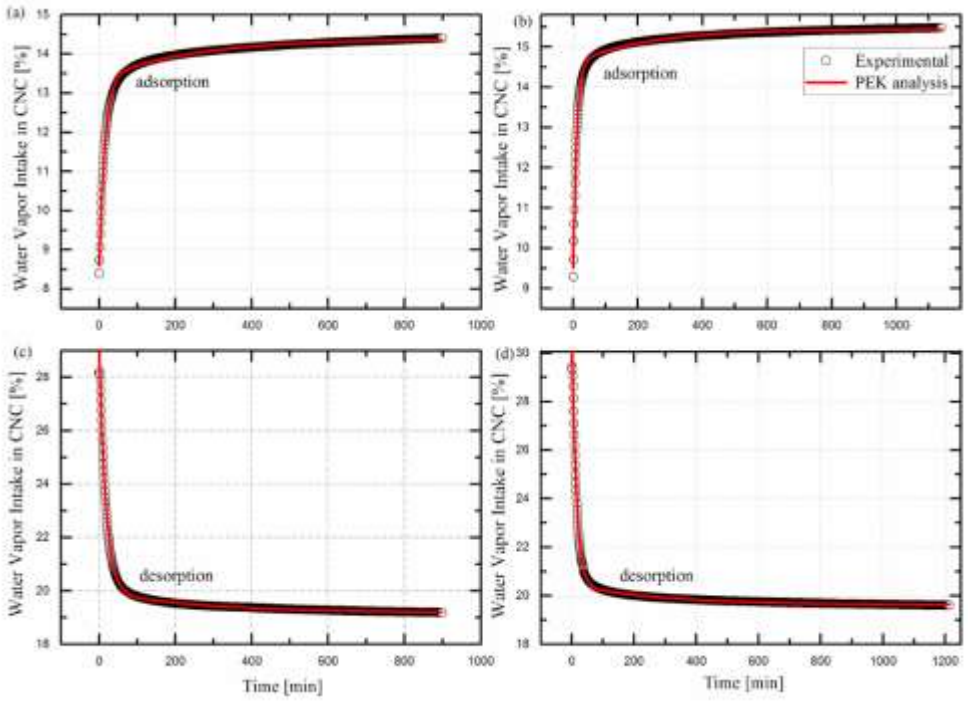

Figure 2.6 PEK simulation of experimental data of adsorption-desorption for self-organized (a) and (c) and shear-oriented (b) and (d) CNC films at high RH 90% and 23°C.

2.4.4 Determination of Coefficient of Hygroscopic Swelling

The coefficient of hygroscopic swelling (CHS) is given by

$$CHS = \frac{\varepsilon}{C} \tag{2.13}$$

where, ε is hygroscopic strain and C is the moisture content in wt.% which is calculated by $\%C$ = (wet weight – dry weight)/ (dry weight) × 100.[70,87,88] To determine the CHS for CNC films, ε measurements (from DIC analysis) were plotted as a function of C (from water uptake using DVS), as shown in Figure 2.7. The slopes of linear trend lines that fitted the plot in Figure 2.7 provide the hygroscopic swelling coefficient (Table 2.5). Although the sorption curve and strain dependence on RH were non-linear, swelling exhibited a linear dependence with moisture content.[89]

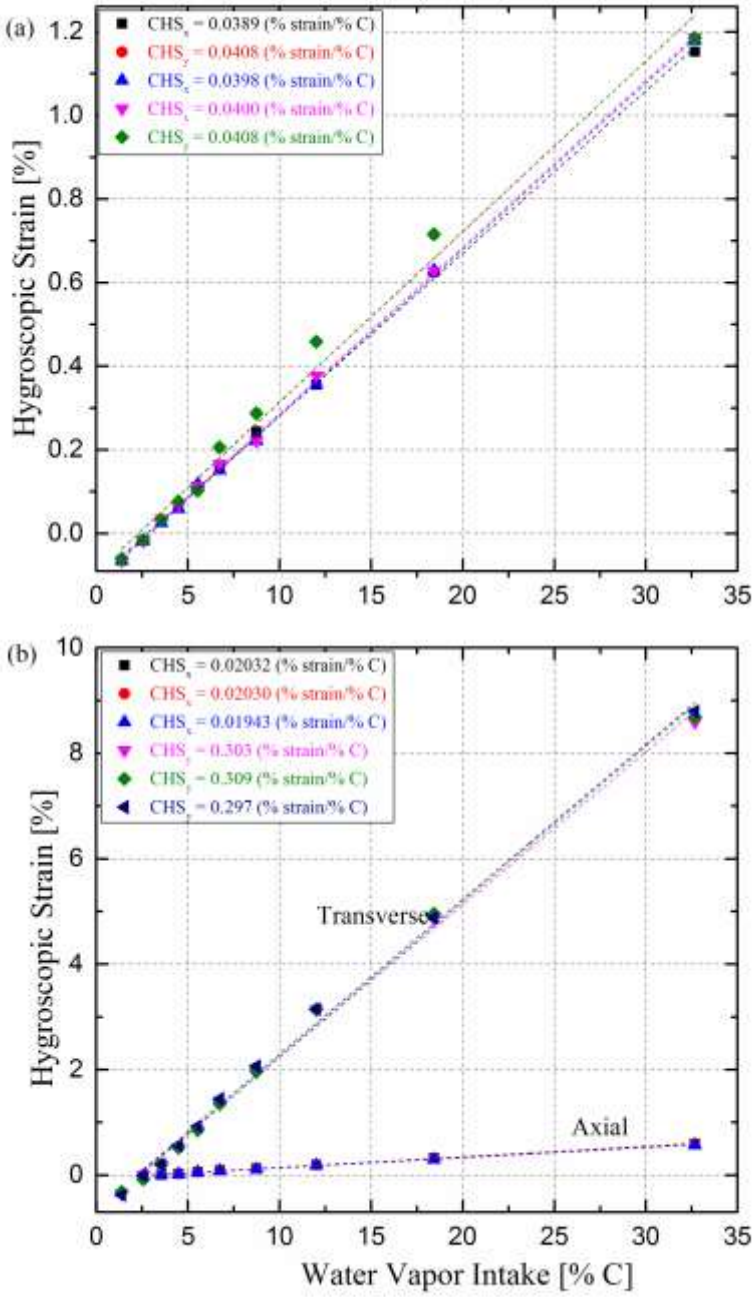

Figure 2.7 Hygroscopic strain in CNC films (a) self-organized (b) shear-oriented as a function of water vapor intake content with different CNC orientations (CHSx = CHSaxial and CHSy = CHStrans).

Table 2.5 Summary of coefficient of hygroscopic swelling of cellulose materials and polymer thin films used in electronic packaging.

Sample		CHS [% strain/% C]	method	Ref.
CNC Film	**self-organized, $S = 0.04$**			this work
	Axial	0.041	CEMDIC	
	Transverse	0.041		
	shear-oriented, $S = 0.8$			
	Axial	0.021	CEMDIC	
	Transverse	0.30		
*Micropillar A	Axial	0.6	**srPCXTM	89
	Transverse	0.8		
*Micropillar B	Axial	0.65	**srPCXTM	89
	Transverse	1.25		
*Micropillar C	Axial	0.28	**srPCXTM	89
	Transverse	0.48		
Polyimide	Axial	0.073	Moiré interferometry	90
	Transverse	0.089		
Woven glass/resin core	Axial	0.125	Moiré interferometry	90
	Transverse	0.067		
Anisotropic conductive film (ACF)	Axial	0.224	Moiré interferometry	90
	Transverse	0.188		

*Secondary cell walls of the latewood (micropillar)
**synchrotron radiation-based Phase Contrast X-ray Tomographic Microscopy

Several self-organized and shear-oriented CNC films were analyzed to determine the hygroscopic swelling behavior and the values of CHS. The self-organized films exhibited in-plane isotropic swelling (i.e., similar values of CHS were observed in the axial and transverse directions) Shear-oriented films showed anisotropic behavior (Table 2.5 and Figure 2.7). CHS values of cellulosic materials such as micropillar A, B and C (secondary cell walls of the latewood) and other polymer thin films used in electronic packaging are shown in Table 2.5. The CHS values in this study were smaller compared to micropillars and other polymer films, such as polyimide (β_x: 0.073 and β_y: 0.089), woven glass/resin core (β_x: 0.125 and β_y: 0.067), anisotropic conductive film (ACF) (β_x: 0.224 and β_y: 0.188).[90] For industrial applications, such as electronic packaging, having a low CHS reduces the risk of failure due to hygroscopic mismatch strains.

2.4.5 Finite Element Method Simulation

To determine and validate moisture diffusion theory as a major mechanism for the occurrence of hygroscopic swelling in CNC films, finite element analysis (FEA) simulation was performed and compared with experimental data (Figure 2.3(d)). By utilizing the diffusion equations, diffusivity and solubility parameters, a numerical model describing ideal Fickian moisture absorption was designed to evaluate water penetration into the films. It was observed that the diffusion coefficient (D) of moisture in the CNCs is not constant, and dependent on RH.[64] Figure 2.8 shows the simulated moisture diffusion profiles of the films at different RH (i.e., 40%, 60%, 70%, 80% and 98%). As the mass concentration of CNC increases, the water vapor diffusion from surface into core of the CNC film also increases along with the RH.

The experimental CHS values (Table 2.5) were averaged, and the amount of water vapor intake (C) was obtained from previous simulation (Figure 2.8). The 15-hour simulation resulted in a semi-empirical hygroscopic strain model for self-organized and shear-oriented CNC films shown in Figure 2.9. Diffusion was deep relative to the film thickness (tens of microns), as water can diffuse 100's of microns into the films over time. Moreover, the films are relatively saturated with little gradient across the film. Thus, dimensional changes due to water vapor are relatively uniform and not a purely surface phenomenon.

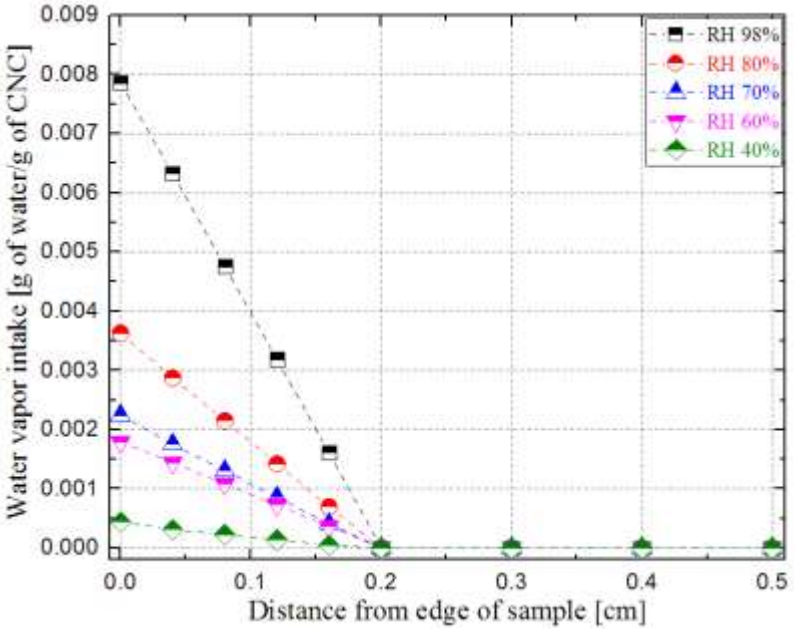

Figure 2.8 Water vapor diffusion profiles as a function of distance from edge of CNC films.

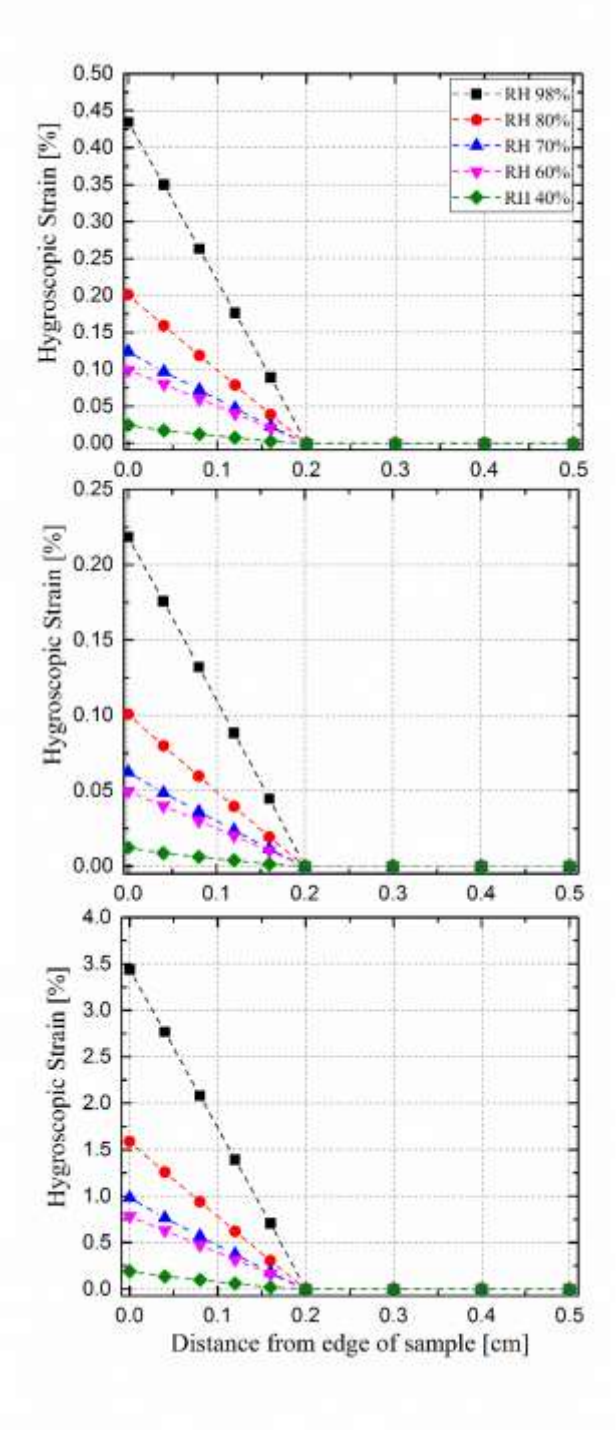

Figure 2.9 Simulation of hygroscopic strain in CNC films at different RH for different CHS of (a) 0.04 %strain/%C for self-organized, (b) 0.02 %strain/%C for shear-oriented in axial direction and (c) 0.30 %strain/%C for shear-oriented in transverse direction.

The total hygroscopic strain as a function of water vapor intake was obtained by the summation of strain to the total water vapor intake by CNC at each individual RH, as shown in Figure 2.10. The simulation results show agreement with the experimental results for hygroscopic strain in self-organized and shear-oriented (transverse and axial direction) CNC films as a function of water vapor intake (Figure 2.7). Thus, moisture diffusion mechanism can solely be considered as the predominant phenomenon of water vapor intake for self-organized and shear-oriented CNC films. Other factors such as capillary flow between the individual CNC crystals within the films could be in principle negligible during hygroscopic swelling.

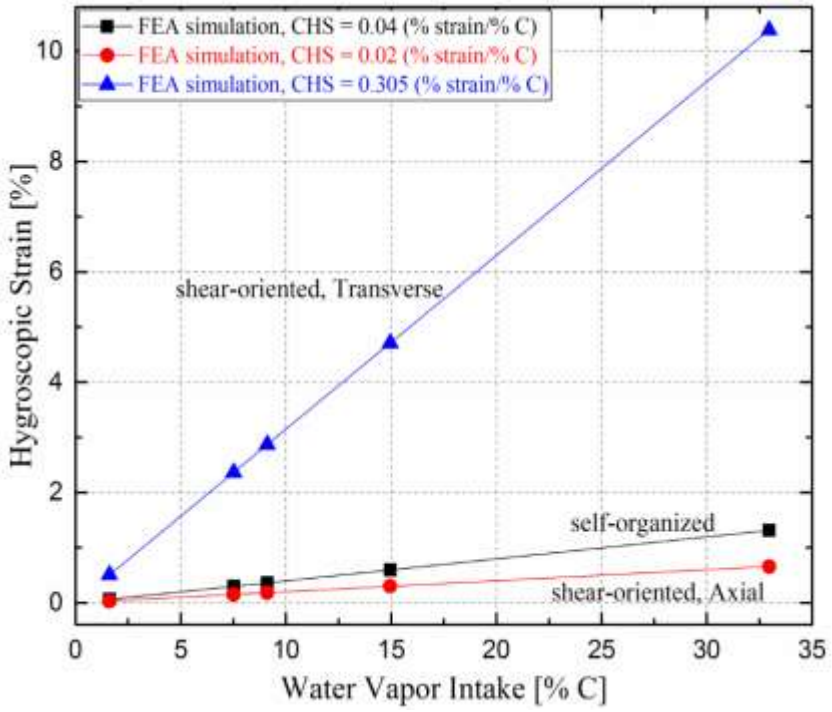

Figure 2.10 FEA simulation of summation of hygroscopic strain as a function of total water vapor intake in CNC films.

2.5 CONCLUSIONS

The in-plane CHS of self-organized and shear-oriented CNC films was determined by optically tracking humidity-driven strain fields in a contact-free manner. Shear-oriented films exhibited a highly anisotropic hygroscopic expansion as compared with the isotropic response determined in self-organized films. The measured CHS values for CNC films were relatively lower than those reported for other cellulosic material such as wood, or commonly used polymer films, such as polyimide. Moisture sorption and kinetic profiles were closely modeled using GAB, PEK, and finite element analysis. Simulations suggested moisture diffusion as the sole mechanism causing hygroscopic swelling in CNC films and other factors such as capillary flow could potentially be neglected. The reduced swelling in CNC films opens a window to control hygroscopic swelling mismatches in future structured cellulosic materials.

CHAPTER 3. EFFECTS OF ASPECT RATIO AND CRYSTAL ORIENTATION OF CELLULOSE NANOCRYSTALS ON PROPERTIES OF POLY(VINYL ALCOHOL) COMPOSITE FIBERS

All lab- work in this chapter was performed by Shikha Shrestha. All analysis was performed by Shikha Shrestha with guidance by Dr. Jeffrey P. Youngblood. All writing was performed by Shikha Shrestha with guidance and editing by Dr. Jeffrey P. Youngblood.

The following chapter contains content reproduced with permission from Shrestha, S.; Montes, F.; Schueneman, G. T.; Snyder, J. F.; Youngblood, J. P. Effects of Aspect Ratio and Crystal Orientation of Cellulose Nanocrystals on Properties of Poly(Vinyl Alcohol) Composite Fibers. *Compos. Sci. Technol.* **2018**, *167*, 482–488. Copyright 2018 Composite Science and Technology

3.1 Introduction

In recent years, polymer nanocomposite fibers have gained popularity due to their significantly improved mechanical performances compared to neat polymer fibers [11,16]. There has been extensive research on using biodegradable or naturally derived reinforcing fillers to develop green nanocomposites in response to the high demand for alternatives to petroleum-based materials [16,91,92]. In this context, cellulose nanocrystals (CNCs) as a reinforcing agent [11,91] has a unique combination of structural properties (e.g., high stiffness and crystallinity [41,93]) and environmental-friendliness (sources include trees, bacteria, and tunicates [11,16]). The highly crystalline CNCs have high modulus (~110 – 220 GPa) and strength (~7 GPa), along with low density (~1.6 g/cm^3) [16,94]. The superior mechanical properties, biocompatibility, sustainability, and cost effectiveness of CNCs account for

them having been incorporated into natural and synthetic polymer matrices, such as cellulose acetate [95], polylactic acid [19], epoxy [20], and polyvinyl alcohol [35] to obtain high-performance nanocomposites.

To take advantage of the high elastic modulus of CNC in the longitudinal axis (~110 – 220 GPa [16,96]), CNC reinforced composite fibers have been produced by various techniques. Clarkson et al. [19] dry spun CNC-polylactic acid fibers, reporting a two-fold increase in modulus at 5 wt.% CNC loading. Chen et al. [95] produced CNC-cellulose acetate fibers by dry spinning with an increase of 137 % in tensile strength and 637 % in elastic modulus. However, the experimental values are generally lower compared to those from micromechanical models in spite of the improved mechanical performance [95,97].

The previous studies showed that optimum interfacial interaction, compatibility and dispersion between CNCs and matrices strongly affected the strength of the polymer composites [92,98]. CNCs are hydrophilic [11,16,94] in nature, and hence result in reduced composite performance when combined with hydrophobic polymers due to low interfacial adhesion, poor stress transfer and severe agglomerations between the two phases [92,99,100]. Thus, water being a preferred medium for processing and dispersing CNCs in composites [101,102] makes water-soluble polyvinyl alcohol (PVA) an ideal matrix to incorporate CNCs. The hydroxyl groups in PVA form strong interfacial hydrogen bonds with CNCs and enhance their mechanical properties. PVA based fibers are commonly used in tissue scaffolding[33], drug delivery[34], cement composites, packaging, and others[36,103]. Incorporating CNCs into PVA fibers, which can have low strength and integrity[98,103], may facilitate improvement in mechanical properties. This approach has been taken by others. Uddin et al. [102] gel spun CNC-PVA fibers, increasing both the tensile strength (1.48 GPa

to 1.89 GPa) and elastic modulus (30 GPa to 56 GPa). Peresin et al. [103] produced CNC-PVA fibers by electrospinning leading to more than three-fold enhancement in mechanical strength at 15% CNC loading than compared to neat PVA fibers.

There have been few studies on aspect ratio effects on cellulose-based PVA composite films [37], and to the best of our knowledge, effects of aspect ratios and types of CNCs on properties of PVA/CNC fibers (in particular) have not been experimentally studied at all. In this work, we studied the preparation and characterization of PVA-CNC fibers produced via dry-jet-wet spinning, which can result in more enhanced molecular alignment than conventional wet spinning [104,105] and uses less specialized equipment than gel-spinning [106]. CNCs hydrolyzed from wood and cotton were reinforced into PVA and spun into fibers. This was subsequently followed by first stage drawing up to draw ratio 2. The goal of this work is to develop industrially scalable process for composite PVA fibers with improved strength and modulus. Furthermore, experimental results for mechanical properties were compared to the predictions from micromechanical models, which accounted for CNC concentration, orientation parameter and aspect ratio.

3.2 Materials and Methods

3.2.1 Materials

PVA with an average molecular weight (M_w) of 89,000 – 98,000 and 99+ % hydrolysis was obtained from Sigma-Aldrich, St. Louis, MO. Aqueous suspensions of CNCs extracted from different sources wood pulp (2015-FPL-CNC-064; 11.8 wt. % in water) and cotton fibers (2015-FPL-CNC-081; 11.4 wt. % in water) were produced by following same process of acid hydrolysis using sulfuric acid [107] to have a similar functionalization. To prepare different lengths from the same source requires digestion to

be more aggressive and longer, which has been shown to introduce differences [16]. These CNCs with different lengths, were provided by the USDA Forest Service-Forest Products Laboratory (FPL), in Madison, WI. The morphology and average diameter of CNCs were characterized using a Philips CM-100 transmission electron microscopy (TEM) operated at 100 kV, spot size 3, 200 μm condenser aperture and 70 μm objective aperture. CNC droplets were placed on 400 mesh formvar/carbon film grid prepared with glow discharge and stained with aqueous uranyl acetate. The average dimensions of CNCs extracted from wood pulp (length: 91.7 ± 35.2 nm; diameter: 8.4 ± 7 nm) and cotton (length: 129.4 ± 34.4 nm; diameter: 9.1 ± 5.8 nm) were determined using ImageJ software. TEM images of CNCs are shown in Figure 3.1. (a) and (b).

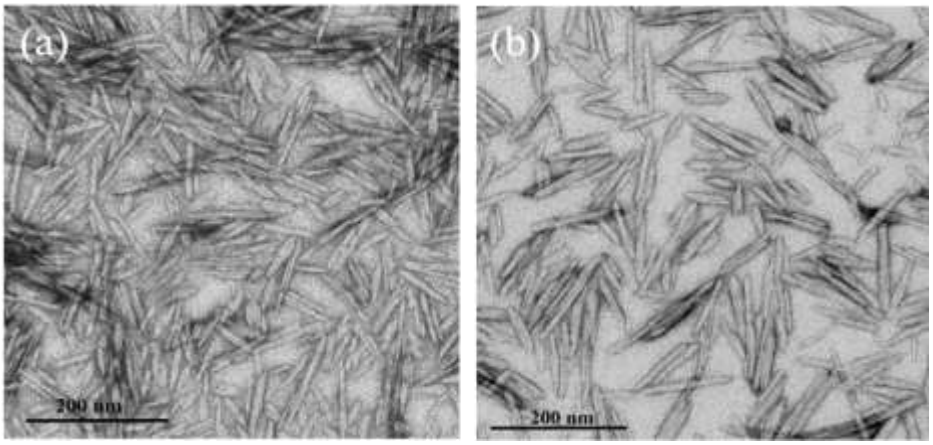

Figure 3.1 Transmission Electron Microscopy (TEM) images of Cellulose Nanocrystals (CNCs) extracted from (a) wood and (b) cotton.

3.2.2 Preparation of PVA/CNC solution

PVA solution was prepared by dissolving PVA powder in nanopure water with constant magnetic stirring at 90 °C for 3 h. As-received CNC suspensions from wood and cotton were added at 0, 5, 10, 15 and 20 wt. % loadings to the solution. The mixture was

transferred to vacuum-assisted rotary evaporator, Yamato RE500, for solvent evaporation. The solvent (water) was evaporated in static rotary mixer (50 rpm, 80 °C and 120 psi) for 3 – 4 h to obtain ~30 wt. % concentration of the final spinning dope.

3.2.3 Formation of PVA/CNC fibers and drawing

The prepared dopes were spun using a method similar to that of Chen et al. [95] A custom-built fiber spinner based on capillary extrusion rheometer [108] with a 30° V-tapered conical shape machined to 4.38 mm was used to insert a 250 μm orifice from Bird Precision, Waltham, MA. This allows fiber processing at high shear rate of $10^5 – 10^6$ s^{-1}. The spinner frame was attached to an MTS Insight, a universal tensile testing machine, to control displacement rate and measure pressure. The spinning dope and the spinneret were heated at the operating temperature of 100 °C and held at the temperature for 2 – 4 h to degas the solution before spinning. The dope was loaded into the spinneret mounted onto the frame and the fibers were spun by pressing shaft into the reservoir. A maximum crosshead speed of 1500 mm/min was applied until the fiber started to extrude from the orifice into the ethanol bath. The air gap between the orifice and the ethanol surface was ~6 inches. The spinning rate was controlled by the amount of force needed to maintain the fiber flow. The initial hand-drawing yielded a maximum draw ratio (DR) of 2. As-spun and wet-drawn fibers were immersed in ethanol for 24 h followed by air drying in fume hood for 24 h. The fibers were subsequently dried in the oven at 105 °C overnight and then stored in a desiccator before characterization.

3.2.4 Microscopy

Surface morphology and diameter of fibers were examined by using the images taken by a Carl Zeiss (Axio Observer A1) inverted optical microscope and measure tool in

ImageJ. Fiber birefringence of CNCs was observed between crossed polarized optical filters, which is considered as a primary indictor for dispersion of CNCs. Moreover, surface and cross-sectional morphologies of fibers, before and after fracture, were determined by using a FEI XL40 scanning electron microscopy. The fiber samples were coated with gold for 30 s at 1 kV, 18 mA, using a SPI-module sputter coater.

3.2.5 2D X-ray Diffraction

A Bruker GADDS 2D X-ray diffractometer (2D XRD) was used to evaluate the degree of orientation of CNCs within the PVA fibers. The 2D XRD used a source of 546 nm Cuα radiation at 30 mA, 20 kV for 900 s and a beam diameter of 500 μm at 6.1 cm from the detector in transmission mode. The fibers were wound, ensuring they were straight and parallel, and glued across a small plastic tab with a hole in the center. The tab with the fiber specimens was attached to a sample holder which was mounted perpendicular to the X-ray beam to allow it to pass through the fibers. The scattering patterns of fibers were recorded on a detector which was placed on the same line along with the sample. The patterns were corrected by subtracting a background of air scattering from the raw data.

The crystal alignment of CNC was quantified by the distribution of intensity (I) with respect to azimuthal angle (ϕ) along the (200) crystal of the cellulose Iβ [109]. Hence, the integration of I versus ϕ was obtained from 0° to 180° around (200) plane at 2θ = 20 – 23°. Similarly, the crystal alignment of PVA was determined by the equatorial diffraction spots corresponding to (200) plane also at 2θ = 20 – 23°[110,111]. Furthermore, Hermans order parameter (S) was calculated assuming axisymmetric orientation where, $S = 0.0$ and $S = 1.0$ represented no preferential orientation and a complete alignment along the axis,

respectively. The equations used in these calculations are listed in Chapter 2 (Equations 2.1 – 2.3).

3.2.6 Mechanical Characterization of fibers

The mechanical properties (elastic modulus, tensile strength, and strain at failure) of a single fiber was measured using a TA Instruments Q800 Dynamic Mechanical Analysis. The fibers were attached on cardboard tabs (gauge lengths of 12 – 15 mm) with high strength epoxy (cured at room temperature) to avoid slippage. At least ten replicates of as-spun and drawn fibers reinforced with both types of CNCs were tested. All samples were stored in a desiccator at 23 °C and 35 % RH for at least 48 h prior to testing. The mechanical properties of single fibers were tested at 0.3 N/min, applied constantly at room temperature until fracture occurred.

3.2.7 Thermal Characterization of fibers

The thermal properties of PVA-CNC fibers were determined using a TA Instruments Q100 Differential Scanning Calorimetry. ~5 mg of fibers was placed in an aluminum pan under nitrogen atmosphere. The heating cycles for the specimens were ranged from 0 °C to 250 °C at 10 °C/min. Thermal stability of the fibers was investigated using a TA Instruments Q50 Thermal Gravimetric Analysis under nitrogen atmosphere. ~10 mg of fibers was placed in a platinum pan and was equilibrated to 100 °C. The fiber specimens were then held isothermally for 30 min to remove residual water completely. Finally, the specimens were heated from 100 °C to 850 °C at 10 °C/min.

3.2.8 Statistical Analysis

The results were analyzed by using one-way analysis of variance (ANOVA) and multiple comparison Tukey tests to check for significance (at $P = 0.05$ level).

3.2.9 Micromechanical Modeling

Elastic modulus of PVA-CNC fibers as a function of CNC loadings was predicted by using numerous models i.e., Isostrain, Isostress, Halpin-Tsai, and Cox-Krenchel models. Isostrain and Isostress models assume that the reinforcing filler of the composites are continuous and perfectly aligned in one direction, and there is perfect adhesion between the filler and the polymer matrix [95].

Isostrain assumes stress is applied parallel to the aligned continuous fillers and is given by:

$$E_c = V_f E_f + V_m E_m \tag{3.1}$$

Isostress assumes stress is applied perpendicular to the aligned continuous fillers and is given by:

$$E_c = \frac{E_f E_m}{V_f E_m + V_m E_f} \tag{3.2}$$

where, E_c, E_f and E_m are the elastic moduli of the composite, filler (CNC) and matrix (PVA), respectively, V_f is the fiber volume fraction, which was determined from weight fractions and the material densities (1.26 g/cm^3 for PVA and 1.6 g/cm^3 for CNC).[16,112] The axial modulus (143 GPa)[16] and transverse modulus (25 GPa)[16] was used for isostrain and isostress, respectively.

The Halpin-Tsai model is used to determine the elastic modulus of a unidirectional short fiber composite. It is based on systems where the reinforcements are fully dispersed, aligned in the longitudinal direction and have quantifiable aspect ratio [113,114]. This model determines the composite modulus by:

$$E_c = E_m\left(\frac{1+\left(2\,{}^{L}/_{D}\right)\eta V_f}{1-\eta V_f}\right) \qquad \text{where,} \quad \eta = \frac{\frac{E_f}{E_m}-1}{\frac{E_f}{E_m}+1} \tag{3.3}$$

The modulus prediction by the Cox-Krenchel model [115,116] was developed based on a classical shear-lag model [117]. This model accounts for both aspect ratio and orientation of inclusions. The following assumptions are made in using the model for composite fibers: (i) fiber and matrix undergo elastic deformation, (ii) no axial loads on the fiber ends and (iii) fully-bonded fiber-matrix interface [115,116]. The model is governed by the equation:

$$E_c = \eta_o \eta_l V_f\, E_f + E_m(1 - V_f\,) \tag{3.4}$$

where, η_o is the orientation factor, which is directly proportional to Hermans order parameter (S). It has values of 0.5 and 1 for in-plane randomly oriented fibers and highly oriented fibers, respectively. η_l is the length factor and can be obtained from shear-lag model:

$$\eta_l = 1 - \frac{\tanh\frac{\beta L}{2}}{\frac{\beta L}{2}} \tag{14.5}$$

$$\frac{\beta L}{2} = 2\frac{L}{D}\sqrt{\frac{G_m}{E_f \ln\frac{\kappa}{V_f}}}$$

G_m is the shear stiffness of the matrix, κ is a constant controlled by the geometrical packing pattern of the fiber, which is assumed to be hexagonal packing in this case with a value of 0.907.[118]

E_c, E_f (143 GPa) [16,95] and E_m (~ 4 GPa, measured in this study) are the elastic moduli of the composite, filler (CNC) and matrix (PVA), respectively, V_f is the fiber volume fraction determined from weight fractions and the material densities (1.26 g/cm^3 for PVA and 1.6 g/cm^3 for CNC) [16,112]. L is the length and D is the diameter of CNC (wood and cotton).

3.3 Results and Discussion

3.3.1 Structure and Morphology of the fibers

Fig.1 shows polarized optical micrographs of as-spun and drawn PVA composite fibers with CNC (from wood and cotton) having concentrations of 0, 5, 10, 15 and 20 wt.%. The polarized micrographs of neat PVA fibers (Figure. 3.2 (a)) show a uniform structure with little birefringence indicating low degree of orientation. CNC reinforced PVA fibers display distinct birefringence under polarized light. It was observed that at low concentrations of 5 wt. % CNC, the fibers showed some local orientation with birefringence (Figure 3.2 (b) and (f)). As the CNC concentration increased, birefringence also increased showing bright colors with iridescent domains (Figure 3.2 (c) – (e) and (g) – (i)) associated with the anisotropy of crystalline CNC [16,119], which indicated well-

dispersed and ordered CNCs within the PVA. These images also revealed large micron scale CNC agglomerates within the PVA matrix, appearing as dark regions.

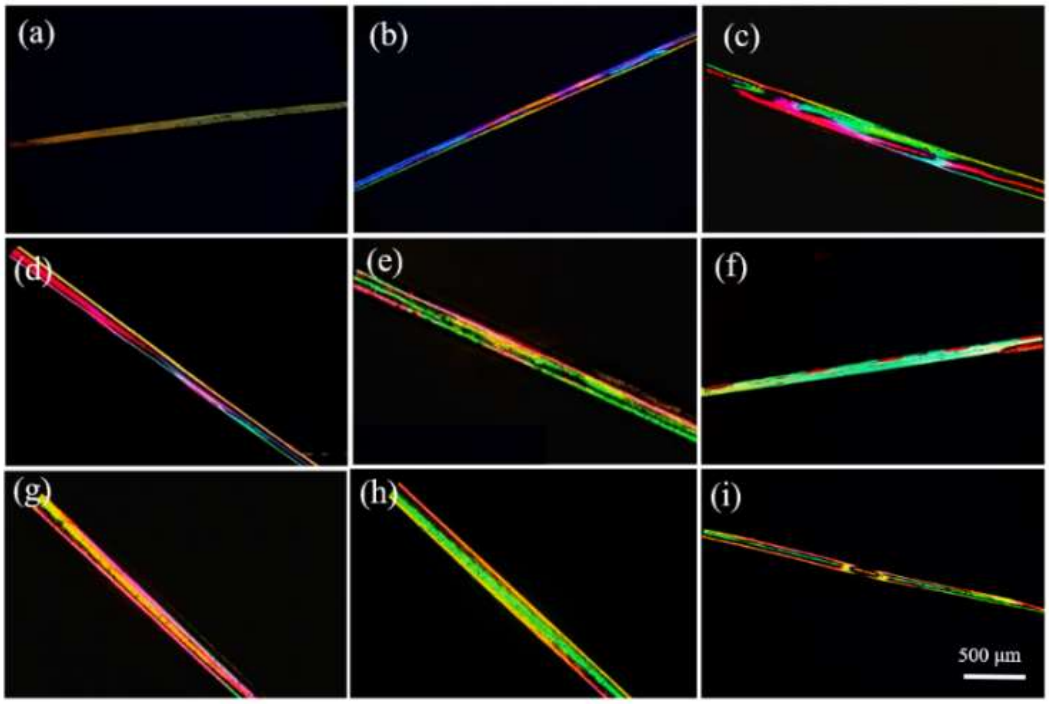

Figure 3.2 Cross polarized optical images of as-spun PVA fibers with (a) 0 wt. % CNC (b) – (e) 5, 10, 15 and 20 wt. % CNC from wood and (f) – (i) 5, 10, 15 and 20 wt. % CNC from cotton.

Figure 3.3 shows SEM images of the surface and cross-section of the spun fibers. The average diameters of fibers with wood CNC varied between 150 and 190 µm and that with CNC cotton varied between 120 and 180 µm. The PVA fibers exhibited smooth surfaces (Figure 3.3 (a)) while PVA-CNC fibers have rough surfaces (Figure 3.3 (b) – (c)) because of CNC reinforcement. Several defects such as, porosity with higher viscosity solutions, surface irregularities, and non-cylindrical cross sections were observed. The non-uniform surfaces occur due to the faster rate of water diffusion out of the fiber than the coagulant diffusion into the fibers resulting in a skinning of more condensed material

surrounding a core of less condensed giving a shell like appearance [120]. More structural defects may be due to the non-homogenous dispersion of CNC in PVA, causing phase separation and limiting the mechanical performances at higher CNC contents. Fig. 2d shows the kidney-shaped cross-section of PVA fibers whose fractured surface was smoother than that of composite fibers. The incorporation of CNCs within the fibers introduced brittleness along with fibrils in their fractured surfaces. This fibrillation morphology was associated with the extent of orientation along the fiber axis, thus leading to higher mechanical properties. The fibrils were observed in fibers with higher CNC loadings but most prominently in the drawn fibers.

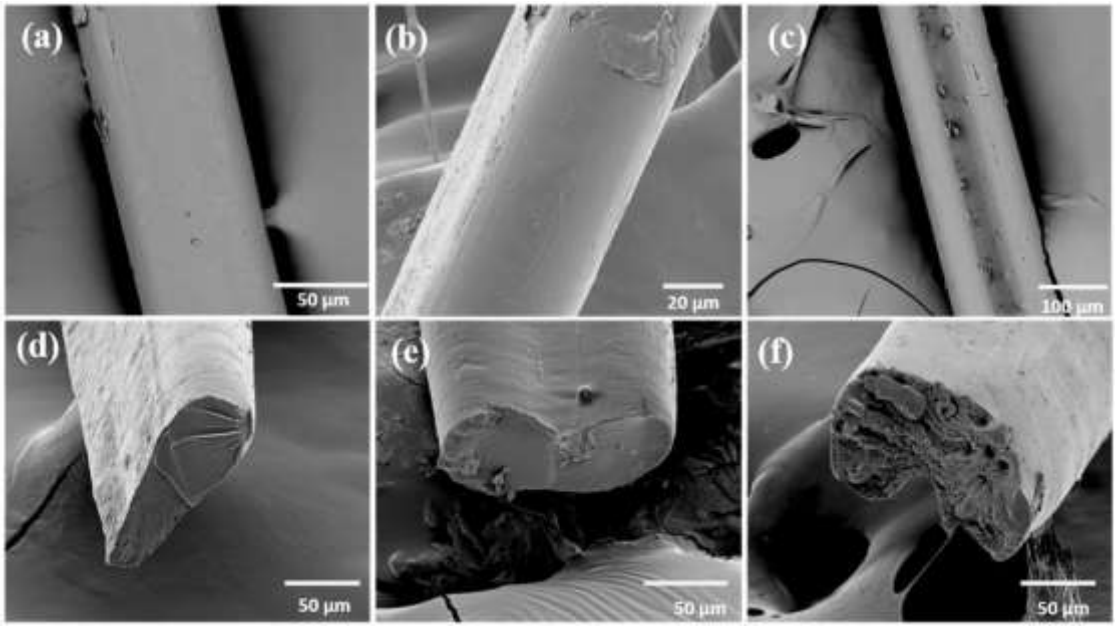

Figure 3.3 SEM images of PVA-CNC fibers (a) – (c) surfaces containing CNC contents of 0, 15 and 20 wt. %, respectively and (d) – (f) cross-sections containing CNC contents of 0, 10 and 20 wt. %, respectively.

3.3.2 Crystal orientation of CNC within PVA/CNC fibers

The degree of CNC alignment along the fiber axis was determined by 2D XRD. Figure 3.4 shows X-ray diffractograms and the integrated intensity of as-spun and drawn fibers with increasing concentration of CNC. As-spun PVA fibers exhibited anisotropic intensity around the broad Debye-Scherrer ring at (200) planes, indicating preferential alignment. Unfortunately, the (200) peak of CNC coincides with the (200) peak of PVA preventing analysis of the individual components [97,102]. However, it can readily be seen that the anisotropy increased with increasing CNC content suggesting alignment of CNC and/or both CNC and PVA in composite fibers is induced by CNC addition. Others have shown that the elongational and shear flows induced by the conical orifice forces anisotropic particles such as CNCs to align in the direction of flow [95]. Furthermore, this alignment of CNCs can induce increased alignment of the fiber matrix polymer as well.

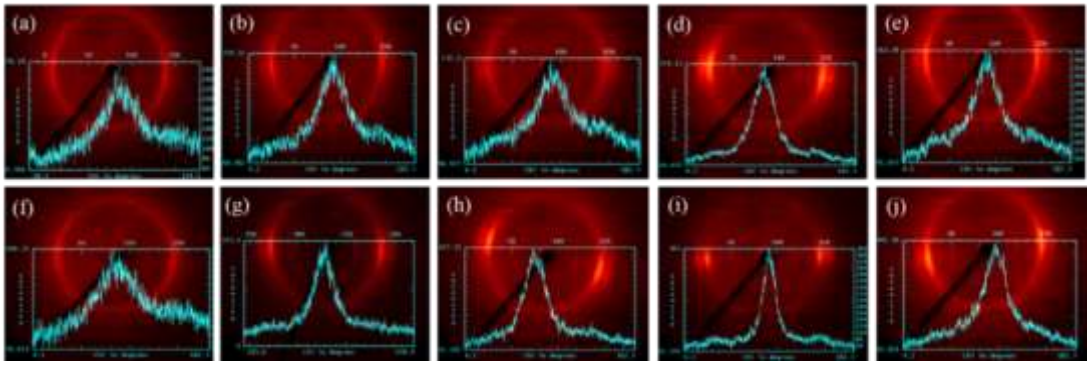

Figure 3.4 2D-XRD diffractograms of PVA-CNC (a) - (e) as-spun fibers with CNC contents of 0, 5, 10, 15 and 20 wt. % and (f) - (j) drawn fibers with CNC contents of 0, 5, 10, 15 and 20 wt. %.

The degree of crystal orientation of the fibers were quantified by calculation of the Hermans order parameter (S) [14]. For PVA fibers, small S values of ~0.2 (as-spun) and

~0.31 (drawn) were observed. As CNC contents were added from 5 to 15 wt.%, the values of S increased (as spun: ~0.33 to 0.61, drawn: ~0.41 to 0.64), indicating improved alignment in the fibers, as shown in Figure 3.5. However, above 15 wt.% CNC, S plateaued and ultimately decreased with further addition of CNCs. This may be due to aggregates of nanocrystals at high concentrations, which hinder alignment in the flow field due to decreased effective aspect ratio as proposed for nanoparticle reinforced composites [95,100]. Furthermore, it was also observed that drawing of the fibers increased the orientation of CNCs along with the matrix PVA in the fiber axis. Since only first stage drawing of as-spun fibers was performed (up to DR = 2) in this study, the maximum drawability of the fibers was not reached, which led to lower order parameters as compared to Peng et al.[100] and Uddin et al.[102]. Second stage post-drawing (wet or hot drawing) is highly recommended for maximum drawability of fibers in achieving higher orientation, and eventually higher order parameters.

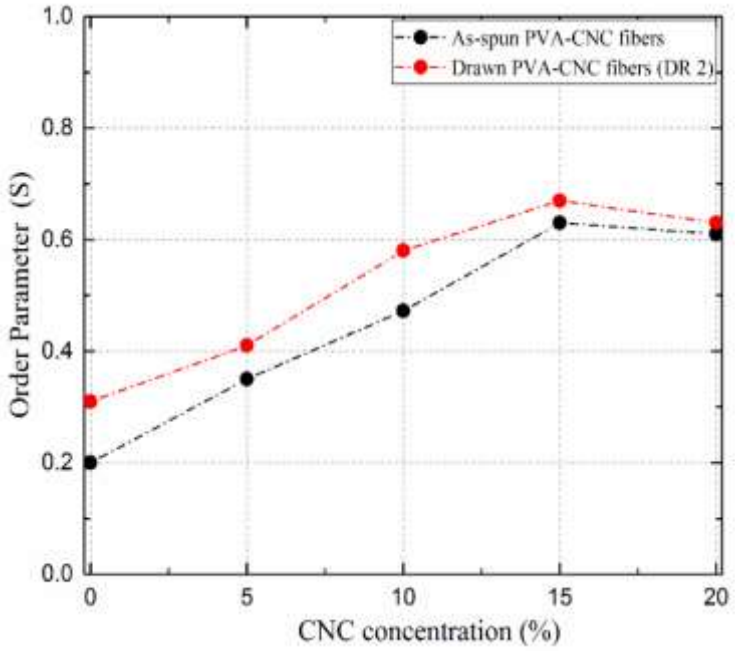

Figure 3.5 Hermans order parameter (S) as a function of CNC content in as-spun and drawn PVA composite fibers.

3.3.3 Thermal Properties of spun fibers

Thermal stability of neat PVA and PVA-CNC (from wood and cotton) fibers was studied using a TGA. It was observed that the onset degradation temperature of PVA-CNC fibers from wood and cotton increased as compared to that of the neat PVA fibers. A similar effect was observed by Yuwawech et al.[37] and Frone et al.[121] in a study on bacterial, nanofibrillated cellulose and microcrystalline cellulose reinforced PVA fibers, respectively. Thermogravimetric and its derivative curves in Figure 3.6 show three degradation steps for the composite fibers. All fiber specimens in Figure 3.6 (a) and (c) show a similar initial weight loss around 100 °C, which was due to evaporation of the absorbed moisture upon heating. After moisture desorption, two major decomposition stages were observed as shown in Figure 3.6 (b) and (d). The second degradation occurred over the temperature

range of 260-360 °C. Hence, the degradation temperature of the fibers increased with the addition of CNCs up to 15%, while their decomposition rate decreased. This indicates that reinforcing CNCs improve thermal stability of the PVA phase. The decrease in decomposition rate is due to the restriction of the mobility of polymer chains (in PVA) and high extent of interaction between reinforced CNC and matrix PVA.[122] This strong interfacial adhesion makes it difficult to break the hydrogen bonding between PVA and CNC. Thus, the degradation temperature in the second transition was increased when CNCs were present. As the CNC loading was increased to 20%, the degradation temperature decreased, indicating a slight reduction in the overall thermal stability of the system. This may be due to agglomeration of CNCs at higher concentration, leading to CNC degradation which is known to occur at these temperatures due to the presence of sulfate half-ester initiating thermal breakdown.[123] However, full dispersion has been shown to mitigate this effect.[123] The third degradation occurred above the temperature 420 °C, which mainly involved the degradation of polyene residue to yield carbon and hydrocarbons.[124–126]

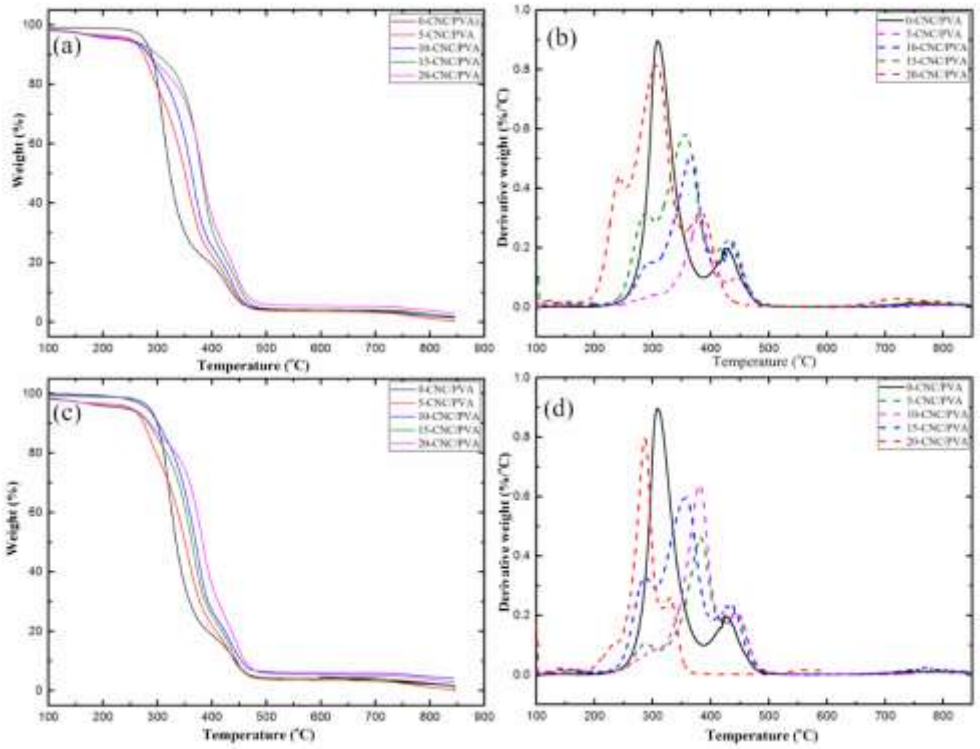

Figure 3.6 (a) - (b) TG and DTG curves of PVA-CNC fibers from wood and (c) - (d) TG and DTG curves of PVA-CNC fibers from cotton.

Thermal properties of the composite fibers were also studied by using a DSC. The values for melting temperature (T_m), heat of fusion (ΔH_m) and the degree of crystallinity (χ_c) are listed in Table 3.1. The degree of crystallinity(χ_c) was calculated by:

$$\chi_c = \frac{\Delta H_m}{w \Delta H_m^o} \tag{3.6}$$

where, ΔH_m^o= 161 J/g is the heat of fusion for 100 % crystalline PVA[26,127] and w is the weight fraction of the PVA matrix in the composite.

DSC measurements were conducted on neat PVA and composite fibers. It was observed that for neat PVA, χ_c and ΔH_m increased significantly after spinning into fibers (Table 3.1). This was attributed to the alignment and improved crystallization of PVA chains within the fibers, when subjected to very high shear stresses during spinning.[128] Table 3.1 showed that the ΔH_m of composite fibers increased when 5 to 15 % CNC was added, regardless of the type of CNC. This phenomenon was ascribed to strong interfacial interactions of the PVA matrix with the number of hydrogen bonding sites. Consequently, CNCs serve as a nucleating agent, which enhance crystallization rate and form larger crystalline domains thus, improving crystallinity of PVA.[124,129,130] Moreover, cotton CNC has higher aspect ratio than wood CNC, so the nucleating effect is more prominent in the former,[131] leading to higher crystallinity. However, as the CNC content was further increased to 20% and above, the ΔH_m and χ_c were decreased (Table 3.1). This showed that the ability of CNC to act as a nucleating agent decreased; hence, CNCs could interfere the regular packing of molecule chain of PVA.[37,132] Furthermore, at higher CNC concentration, it was most likely that the CNCs were aggregated and there was lower interfacial area between PVA and CNC.[37] On the other hand, the T_m of fibers with both types of CNC at different loadings remained nearly constant.

Table 3.1 Results from DSC measurement of PVA and PVA-CNC composite fibers

Sample	CNC content (wt. %)	T_m (°C)	ΔH_m (J/g)	Degree of crystallinity χ_c (%)
PVA Fiber	0	226.5	49.5	31.1
PVA-CNC (Wood)	5	225.7	53	34.7
	10	226.5	53.2	36.1
	15	225.9	56.4	41.4
	20	224.1	38.3	29.7
PVA-CNC (Cotton)	5	225.1	54.7	37.0
	10	227.4	59.6	41.1
	15	226.6	63.2	46.2
	20	226.2	47.5	37.1

3.3.4 Mechanical Properties of spun fibers

The mechanical properties of the fibers with different aspect ratios of CNCs are shown in Figure 3.7. It was observed that regardless of CNC types (wood or cotton), elastic modulus (E) and tensile strength (σ_{TS}) of the fibers increased along with CNC content at the expense of their strain-to-failure (ε_F). The neat as-spun PVA fiber had an E of 3.24 GPa, σ_{TS} of 100.01 MPa and reached its ε_F at 28.31%. The E and σ_{TS} increased after adding 5 – 15 % CNC (of both types) and reached their highest values at 15 wt.% i.e., E from 3.24 to 10.76 GPa (wood) and 14.31 GPa (cotton) ($P \leq 0.05$); σ_{TS} from 100.01 to 230.86 MPa (wood) and 274.38 MPa (cotton) ($P \leq 0.05$). This behavior may be due to the effective stress transfer from the PVA to CNC and formation of a continuous percolation CNC network via hydrogen bonding [37,99]. From Figure 3.7 (a) – (b), it was observed that

the E and σ_{TS} of fibers with cotton CNC are higher than that of the fibers with wood CNC at the same CNC content. This is likely because the CNC with higher aspect ratio is expected to significantly improve the mechanical properties [133]. Also, as seen with the increase in crystallinity of PVA (shown by DSC data in Table 3.1) by the cotton-based CNC, CNC with high aspect ratio can have strong reinforcing impact driven by crystallization of the matrix, which can also enhance the mechanical properties of the fibers [102]. However, at higher CNC content (> 15 wt.%), E and σ_{TS} tend to decrease. It is probable that at higher CNC loadings, the defects such as, agglomerations, voids, and uneven cross sections increase, as shown by SEM images, leading to premature failure of the fibers. There exists poor stress transfer across the interphase that resulted from CNC aggregates and voids [95,134,135], contributing to decrease in modulus. On the other hand, it was observed that the ε_F of the fibers continuously decreased with the addition of CNCs. This is attributed to the strong interactions between CNC and PVA limiting the molecular movement of the PVA matrix [136].

The fibers were subsequently wet-drawn (at a constant DR = 2) directly after spinning (i.e., without drying and reswelling fibers), which immensely affects the mechanical properties. As shown in Figure 3.7, E and σ_{TS} for neat PVA and PVA-CNC fibers increased significantly after drawing. The maximum E and σ_{TS} achieved (at 15 wt.% CNC content) was 15.02 GPa, 272.65 MPa (wood) and 18.08 GPa, 356.34 MPa (cotton), respectively ($P \leq 0.05$). Whereas, ε_F showed continuous decrease with drawing for all the fibers. The high mechanical properties of drawn fibers were induced not only by a reinforcing effect of CNCs, but also by a degree of alignment of the polymer chains along the fiber axis that originated during wet-drawing [137].

The mechanical properties of the fibers are strongly affected by the orientation of CNC. E and σ_{TS} curves are directly correlated to the order parameter curve as shown in Figure 3.5. Hence, increasing CNC alignment is an important parameter to improve mechanical properties. The E of CNC in the longitudinal and transverse directions are 110 – 220 GPa and 2 – 50 GPa [16,96], respectively, which explains the increase in E with increasing order parameter. As the loading of CNC increases, the CNCs become more oriented along the fiber axis due to a strong reinforcement of CNC into PVA. However, after the maximum value of orientation is reached, the order parameter curve immediately plateaus and further addition of CNCs reduces the orientation decreasing the mechanical performances.

The improvement in mechanical properties of PVA-CNC fibers in this study is similar or higher than that reported in previous studies [102,138]. Maximum improvements in σ_{TS} of 100.03 % (as-spun) and 147.5 % (drawn) for wood CNC and 153.60 % (as-spun) and 190.43 % (drawn) for cotton CNC composite fibers were achieved. Also, maximum improvements in E of 235.38 % (as-spun) and 401.94 % (drawn) for wood CNC and 363.96 % (as-spun) and 519.57 % (drawn) for cotton CNC composite fibers were achieved. Uddin et al. [102] gel-spun PVA composite fibers up to 30 wt.% CNC, followed by hot drawing. There was an increase in modulus and strength at 5 wt.% loading of CNC by 86% and 27%, respectively as compared to the neat PVA fibers [102]. Peng et al.,[100] and Liu et al.,[138] showed a maximum increase of 220% and 222.9% in modulus as compared to neat PVA fibers at 5 wt.% inclusion of CNC. The results are similar to the as-spun PVA-CNC fibers at 15 wt.% CNC content in this study. The differences observed in the reinforcing effects in these fibers could be due to the differences in CNC aspect ratios or drawing.

Furthermore, it was observed that the optimum concentration at which the maximum mechanical properties were achieved is higher in this study than the previously mentioned studies [100,102,138]. This implies that higher shear rates lead to better reinforcing potential of CNCs i.e. increase in CNC alignment along the fiber axis direction [95].

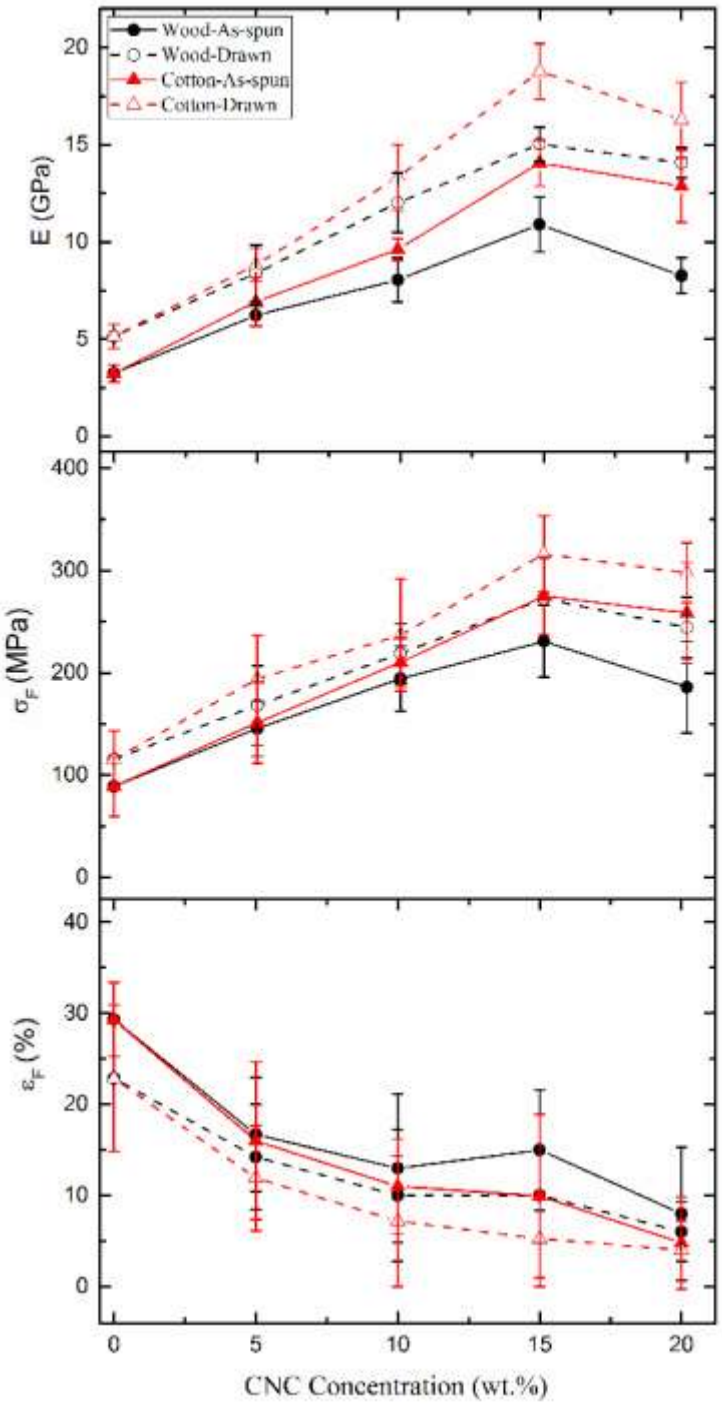

Figure 3.7 Mechanical properties of as-spun and drawn PVA-CNC composite fibers: (a) elastic modulus, (b) tensile strength and (c) strain at break as a function of concentration of CNC.

3.3.5 Micromechanical Modeling of PVA/CNC fibers

The comparison between elastic modulus from experimental data and predictions by the Isostrain, Isostress, Halpin-Tsai model and Cox-Krenchel model is shown in Figure 3.8. The average aspect ratio values were determined by data collected from TEM and calculated to be 11.7 and 14.5 for CNCs extracted from wood and cotton, respectively.

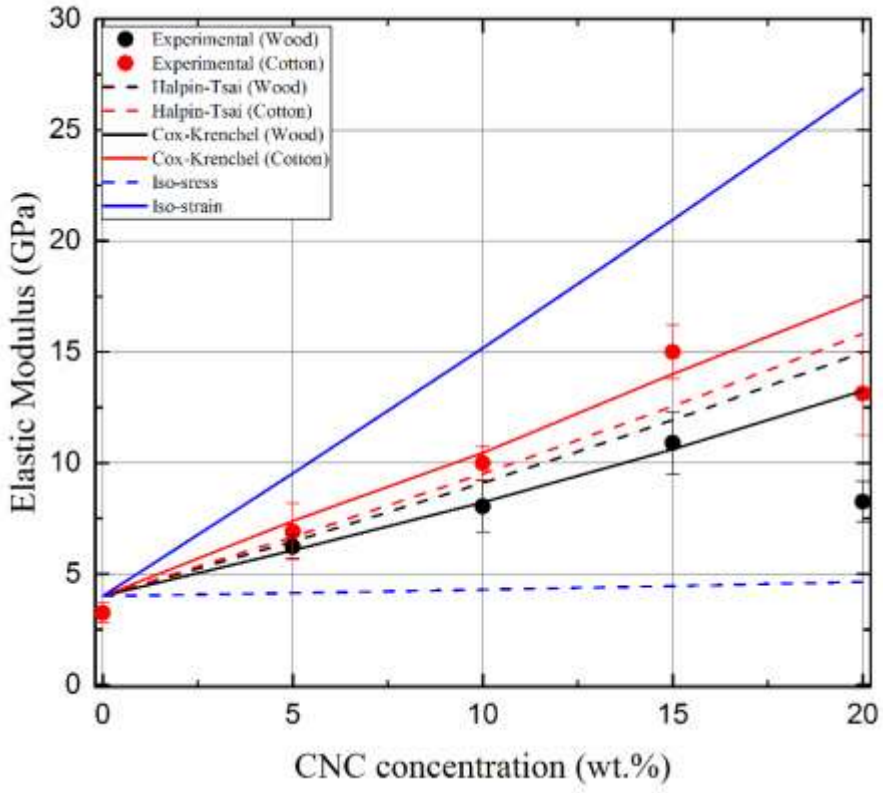

Figure 3.8 Experimental and predicted values of elastic modulus for as-spun PVA-CNC fibers by Isostress, Isostrain, Halpin-Tsai and Cox-Krenchel model.

Isostrain and Isostress models provide the widest upper and lower bounds for the PVA-CNC fiber performance, respectively. The Halpin-Tsai model showed an approximate prediction of the elastic modulus of fibers but only up to 10 – 12 wt.% of CNC contents. The experimental data was higher in the fibers reinforced with cotton CNC than that predicted by the model at 15 wt.% CNC. The increase in modulus may be due to

increased crystallinity of PVA induced by the CNCs. On contrary, the model over-predicted the performance of the fibers above 15 wt.%. The divergence at higher CNC content was possibly due to the agglomerations between CNCs resulting in a larger sized reinforcement, which cannot be predicted by any model. This significantly lowers filler-matrix surface area leading to decrease in mechanical properties [139].

The Cox-Krenchel model is based on the aligned reinforcing phase along the fiber axis and its aspect ratio [95,115,116]. The prediction by this model showed the best agreement with the experimental modulus than any other models used in this study. Moreover, the model assumed perfect elastic adhesion between the filler and matrix. Thus, the good fit is indicative of a high degree of interaction between CNC and PVA. Hence, the PVA composite fibers showed an improved dispersion along with higher elastic modulus [140]. However, the deviation at the higher CNC content is related with the defects, such as CNC agglomerates as discussed above.

The general fitting of the models demonstrated the importance of good dispersion of CNCs, alignment of reinforcement and matrix (CNC/PVA) and crystallinity of the matrix (which is affected by the CNC content) to improve the mechanical properties of the fibers [95,97]. Further increment of CNC above its optimum concentration decreases CNC dispersion, which limits improvement of modulus. Importantly, the models indicate that shear-lag behavior is dominant.

3.4 Conclusions

CNCs derived from wood pulp and cotton were reinforced into PVA to produce continuous fibers by dry-jet-wet spinning, followed by wet-drawing. Tensile strength and elastic modulus of the fibers were greatly improved by addition both types CNC up to 15

wt.%, after which the properties plateaued or decreased, possibly due to defect formation from a loss in CNC dispersion. The drawn fibers also exhibited highly oriented CNC and excellent mechanical properties. It was observed that the lengths of CNCs have significant beneficial effect on the mechanical strength of the matrix. Micromechanical models suggest that the increase in elastic modulus of PVA-CNC fiber resulted from high interfacial interaction between CNC and PVA, increased orientation parameter, greater aspect ratios and that the CNCs observed shear-lag behavior. Overall, this study suggested that cotton CNC exhibited better intrinsic properties than wood CNC, in terms of reinforcing PVA, due to their modest increase in aspect ratios that have outsized effect owing to the structural arrangement of the CNC in the polymer (i.e. shear-lag rather than percolation).

CHAPTER 4. THERMAL AND MECHANICAL PROPERTY EFFECTS OF TEMPO-OXIDIZED CELLULOSE NANOFIBRIL ON EPOXY USING A FACILE, AQUEOUS SURFACE MODIFICATION PROCESS

All lab- work except surface modification of CNF and SEM images was performed by Shikha Shrestha. All analysis was performed by Shikha Shrestha with guidance by Dr. Jeffrey P. Youngblood. All writing was performed by Shikha Shrestha with guidance and editing by Dr. Jeffrey P. Youngblood.

4.1 Introduction

Fiber-reinforced polymer nanocomposites are envisioned for use in many advanced engineering structural industries, such as aerospace, automotive, packaging, and construction due to their unique combinations of high strength and stiffness with low density[4–6]. Generally, polymer nanocomposites are filled with high strength fibers, like glass[1], and carbon[2,3] to improve their intrinsic properties. In recent years, due to the increasing concern for environmental conservation, there has been extensive interest in biopolymer-based nanocomposites, and cellulose nanomaterials (CNs) have potential as renewable and sustainable polymer reinforcement used in fiber [18], films[141,142], cement[143], and composites[4,29]. These nanoparticles are cellulose-based (sources include trees, tunicates, and bacteria[8]), and have unique characteristics like superior mechanical properties, high aspect ratios, low density, low thermal and hygroscopic expansion, and chemical functionality at the surface[8,93,144]. Due to these attractive traits, CNs have been widely incorporated into a variety of thermoplastics such as polyethylene, polypropylene, [104] and polyvinyl alcohol,[18] and thermosets such as epoxy and polyurethane.[21,29]

Cellulose nanofibrils (CNFs) are one type of cellulose-based nanomaterials with long fibrils (width: ~ 4 – 20 nm; length: > 1 µm length[22]) forming a network structure and having remarkable mechanical properties. These nanofibrils are typically extracted from wood pulp either by mechanical grinding, high-shear homogenization or TEMPO-mediated oxidation[23–25]. CNFs are comprised of both amorphous and crystalline cellulosic regions and possess characteristics such as high surface area (with a web-like structure), high aspect ratio, light weight and active interfaces[27,145], which make them a potential reinforcing material for polymer nanocomposites. However, using CNF as nanofiller exhibit some drawbacks, associated with limited compatibility between the hydrophilic CNFs and the common hydrophobic polymer matrices along with poor dispersion of nanofibrils[6,146]. This leads to inferior mechanical strength of resulting nanocomposites. Hence, to improve the compatibility between fillers and matrices, various types of surface modifications can be used via silylation, esterification and polymer grafting[25,147,148].

Epoxy is a commonly used class of thermoset polymers with excellent mechanical performance, low shrinkage and resistance to degradation (corrosion due to weather and solvent). Due to these comprehensive properties, epoxy is widely used in many industries, for example, coatings, adhesives, electronics, and structural composites. However, the cured epoxy systems tend to exhibit brittle fracture behavior with low impact strength, fracture toughness and poor crack growth resistance, which limits their high-performance applications[149,150]. Since epoxy is one of the important fiber-reinforced matrices, incorporation of nanofillers at lower concentration can improve overall properties of nanocomposite. Previously, there have been several studies on utilizing various types of organic and inorganic nanofillers, for instance nanoclay, carbon nanotubes, metal-oxides,

and cellulose nanocrystals (CNCs) in epoxy resins[29,149]. However, there are only a few reports in literature that have used modified CNFs in epoxy to enhance their properties. CNFs used in these studies were hydrophobized by using surfactants to emulsify either CNF or matrix to create dispersion[10]. This modification requires extensive purification to remove excess surfactant. Another method used for CNF modification is solvent exchange of water in CNFs to DMF or other co-solvent, which is removed during molding[27,151]. These methods exhibit challenges such as environmental emission of volatile organic compounds (VOC), multiple purification steps, toxic catalysts, and low yield of modified products. However, modifying CNFs by altering their surface chemistry with a water-based method can eliminate the use of solvent or dispersant during processing and reduce VOC emission. To the best of our knowledge, there has not been any study exploring the effect of surface modification of CNF extracted from wood pulp on the dispersion and overall properties of epoxy nanocomposites.

In this work, a CNF/epoxy system is explored. It is known that CNFs with high dispersion and high aspect ratio exhibit stronger reinforcing effects[28]. To use these properties towards our advantage, TEMPO-oxidized CNF (TOCNF) was reinforced into epoxy and its influence on properties was explored. TOCNF was successfully surface modified to enhance the dispersibility and reduce its hydrophilicity for the epoxy matrix used in this study. Furthermore, for comparative performance study of modified CNF, unmodified CNF was also incorporated into epoxy. Finally, the effects of different contents of CNFs on mechanical, thermal, and morphological properties were compared and analyzed.

4.2 Materials and methods

4.2.1 Materials

Tannic acid, hexadecylamine (98%), and HEPES (4-(2-hydroxyethyl)-1-piperazineethanesulfonic acid) were purchased from Sigma Aldrich, St. Louis, MO, USA. Epoxy resin consisting of 150 thick epoxy (diglycidyl ether of Bisphenol-A (DGEBA)) and 55 polyamide hardener were purchased from US Composites, West Palm Beach, FL, USA. Ethanol (200 proof) was purchased from VWR, West Chester, PA, USA. Never dried, pristine 0.82 wt. % aqueous suspension of TEMPO-oxidized CNF (batch: 2014-FPL-CNF-080) was purchased from University of Maine and manufactured by USDA Forest Services-Forest Products Laboratory (FPL), Madison, WI, USA. The morphology of CNFs was characterized using a Philips CM-100 transmission electron microscopy (TEM) operated at 100 kV, spot size 3, 200 µm condenser aperture and 70 µm objective aperture and the image is shown in Fig. S1. All chemicals were used as active ingredients without any purification.

4.2.2 Surface modification of CNF

TOCNF was modified with a water-based method for the first time using the procedure by Hu et al.[152], which was performed to functionalize CNCs. All steps are performed at ambient conditions. 0.467 g of HEPES was dissolved in ~250 g of as-received CNF suspension, and the pH was adjusted to 8.0 with NaOH solution. Subsequently, 0.1 g of tannic acid (TA) was added to the suspension and stirred mechanically at 900 rpm for 10 h at room temperature. Next, 4.0 g of hexadecylamine (HDA) was dissolved in 50 g of ethanol, which was mixed with CNF-TA suspension at 1500 rpm for 12 h. CNF-TA-HDA was concentrated by centrifuging under 4000 rpm for 30 min and was washed three times

with water purified to at least 18.2 MΩ-cm resistivity followed by anhydrous ethanol. The product (CNF-TA-HDA) was separated from the liquid phase by filtering the top of the water as the hydrophobic particles tend to float. The yield product was dried at 65 °C and was stored for fabrication and characterization. The detailed schematic and reaction schemes of the CNF modification are shown in Figure 4.1 (a) and (b), respectively. Further details on the synthesis can be found in the cited reference.[152]

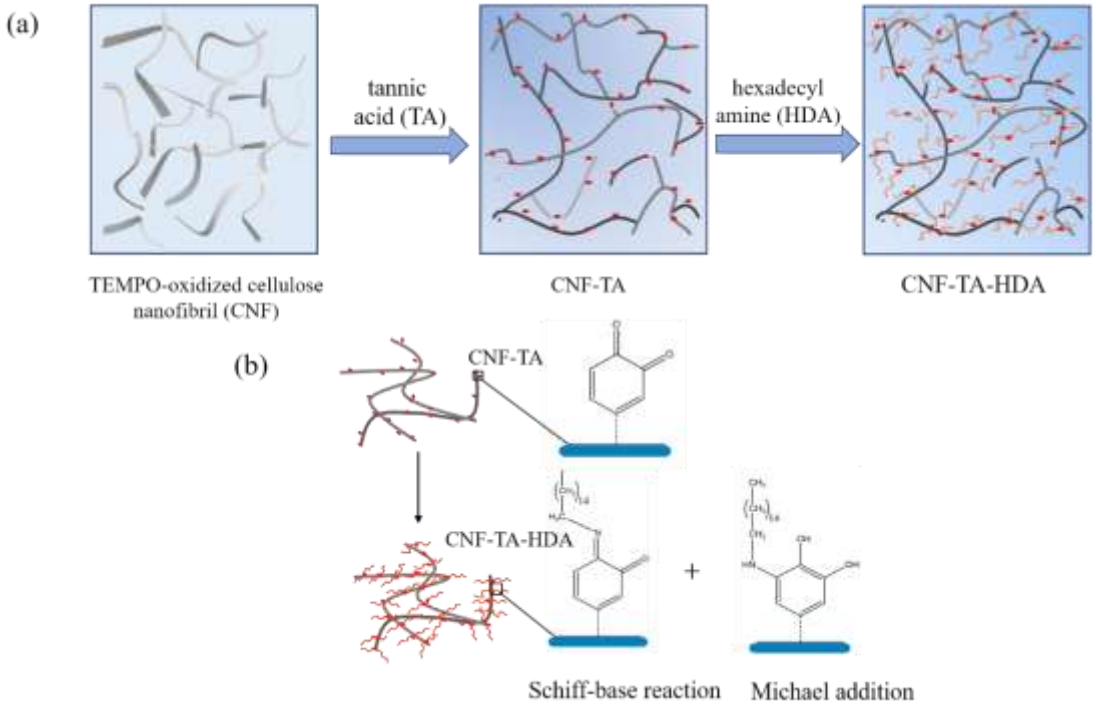

Figure 4.1 Schematic showing surface modification of CNFs: (a) detail steps in the one-pot water-based reaction and (b) chemical reactivity pathway for modification with tannic acid followed by hexadecylamine addition (not drawn to scale).[152]

4.2.3 Fabrication of CNF/epoxy nanocomposites

The epoxy nanocomposites were prepared in a method similar to that of Peng et al.[29,153]. 0, 0.3, 0.5, 1 and 3 wt.% dried CNFs were first dispersed in acetone and sonicated

using a Branson Ultrasonicator, S-250D (ultrasonic horn, output power ~ 200 watts, pulse on/off mode for 1 s and amplitude of 30%) for 2 min. The 150-thick epoxy was then added to the unmodified (um-) and modified (m-) CNF suspensions and sonicated to obtain even dispersion. Subsequently, the acetone was removed by heating the mixture in a vacuum oven at 60 °C for 24 h. After solvent removal, 556 polyamide hardener was added to the CNF/epoxy mixture. The ratio of the epoxy to hardener was 2:1 by weight as suggested by the supplier. The hardener was mixed homogenously with CNF/epoxy by using a FlackTek Inc. (DAC 400.1 FVZ) planetary centrifugal mixer at 2500 rpm for 2 min. The samples were degassed for 30 to 45 min under low vacuum. Neat epoxy was also prepared by mixing epoxy and hardener in the ratio 2:1 and by following the same procedure as mentioned for nanocomposites. All samples were cured at 60 °C for 1 h, 80 °C for 2 h and 125 °C for 3 h. The detailed schematic is shown in Figure 4.2.

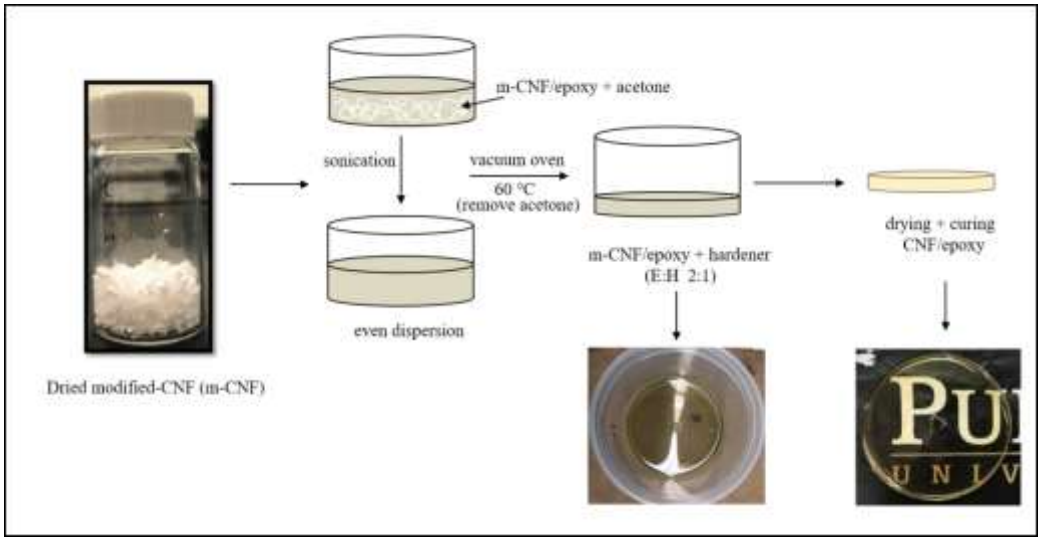

Figure 4.2 Detail schematic showing the fabrication of CNF/epoxy nanocomposites.

4.2.4 UV-Vis spectroscopy

Light transmittance of the neat epoxy and CNF/epoxy nanocomposites were measured by using a Varian Cary 50 Bio UV-Vis spectroscopy over the wavelength from 350 nm to 750 nm.

4.2.5 Microscopy

The dispersion of CNFs in the epoxy was qualitatively analyzed by taking the images of the samples in between cross polarized optical filters using a Carl Zeiss (Axio Observer A1) inverted optical microscope in transmission mode. The tensile fractured surfaces of nanocomposites were studied by using a FEI XL40 field emission scanning electron microscopy (FE-SEM) operating in a high vacuum mode at accelerating voltage of 10 kV. The samples were coated with gold for 30 s at 1 kV, 18 mA, using a SPI-module sputter coater.

4.2.6 Tensile Testing

The tensile properties of epoxy nanocomposites filled with modified or unmodified (m/um) -CNF were determined by using an MTS Insight, a universal tensile testing machine. The specimens were laser cut into a dumbbell-shape, following ASTM 638-10 Type IV dimensions proportionally decreased to half. The tests were performed at a crosshead speed of 5 mm/min until failure of specimens occurred. Eight to ten replicates for each type of nanocomposites were tested.

4.2.7 Thermal Testing

The thermal behaviors of the epoxy and its nanocomposites were determined by dynamic scanning calorimetry (DSC) and thermal gravimetric analysis (TGA). DSC

measurements were performed using a TA Instruments Q2000 machine in nitrogen. The samples were equilibrated at 150 °C for 5 mins to remove the thermal history, then cooled to 0 °C at 10 °C/min. Subsequently, the samples were heated to 200 °C at 5 °C/min, and the final ramp was used to calculate T_g. Thermal stability of the nanocomposites was investigated using a TA Instruments Q50 TGA under nitrogen and the samples were scanned over temperatures from 25 °C to 650 °C at 10 °C/min.

4.2.8 Statistical Analysis

The results from nanocomposite characterization was analyzed by using one-way analysis of variance (ANOVA) and multiple comparison Tukey tests to check for significance (at $P = 0.05$).

4.3 Results and Discussion

4.3.1 Dispersion of CNF in epoxy

Polarized light microscopy (PLM) images are used as a primary indicator to analyze the dispersion of CNFs in epoxy. Between crossed polarizers, the undispersed m-CNF aggregates show birefringent domains at a certain concentration due to the ordering of crystalline parts[154] of nanofibrils, which are depicted as bright white regions in Figure 4.3. On the other hand, Figure 4.3 (f) indicated that the um-CNF did not disperse in acetone (commonly used as thinner/solvent for epoxy) nor in epoxy but formed solid CNF droplets (due to higher surface tension) when the acetone evaporated. These CNFs tend to block the light, thus, appear as dark black dots. These images are qualitatively compared to the neat epoxy with no birefringence (Figure 4.3 (a)). Furthermore, the cured epoxy nanocomposites were visually analyzed by the digital images in Figure 4.3 (insets). For m-

CNF nanocomposites, the color of the specimens became darker with uniform brownish tint as the content of m-CNF increased. Although distinct CNF aggregates were observed between crossed polarizers at higher concentration, the samples still maintained transparency. This phenomenon was also observed by Yano et al.[155], where cellulose/epoxy composites at high filler content transmitted ~80 % visible light, indicating that even aggregated cellulosic materials appear transparent. When adding um-CNF to the epoxy, the specimen showed large CNF particulates and became a little cloudy in appearance. This is likely due to the aggregation of undispersed um-CNFs, leading to scattering of light.

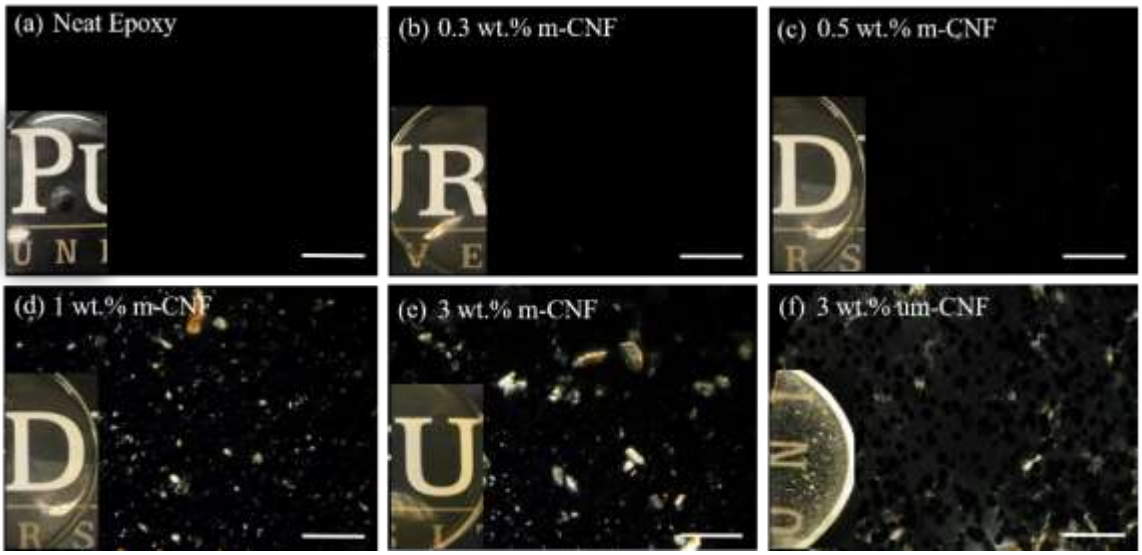

Figure 4.3 (a) – (f) Polarized light microscopy images and digital images (insets) of epoxy nanocomposites with m-CNF and um-CNF. The scale bar is 100 μm.

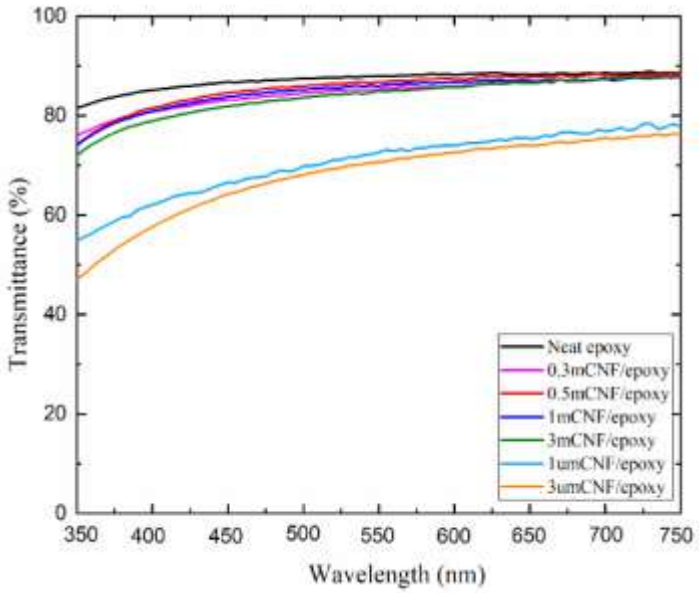

Figure 4.4 UV-Vis transmittance spectra of neat epoxy and epoxy/CNF nanocomposites.

Optical transmittance spectra of CNF/epoxy nanocomposites are shown in Figure 4.4. The light transmittance of neat epoxy was at a high of 87.5 % at 600 nm and lowered slightly to ~85 % when m-CNFs was added to the epoxy. However, the transmittance of um-CNF/epoxy decreased by a larger amount to 68 – 70 %. This similar trend was observed in optical transparency images in Figure 4.3 (insets). From these transparency results along with polarized light micrographs, it can be concluded that the m-CNF led to better dispersion than um-CNF in epoxy and this was mainly due to the surface modification of CNFs.

4.3.2 Fracture surface morphology of CNF/epoxy nanocomposites

To determine dispersion and interfacial bonding of m/um-CNF and evaluate their effects on epoxy nanocomposites, tensile fracture surfaces of the specimens were studied using FE-SEM images shown in Figure 4.5. Neat epoxy showed a smooth, homogenous and glassy fracture surface with some wavy-line patterns as observed in Figure 4.5 (a),

indicating its brittle nature with weak resistance towards crack propagation. Thus, relatively less energy was required for tensile failure, which was also suggested by other epoxy studies[6,27,156]. In contrast, the SEM micrographs of epoxy nanocomposites with CNFs, from Figure 4.5 (b) – (i), displayed irregular fracture surfaces. As expected, um-CNF showed poor dispersion in epoxy due to its incompatibility with hydrophobic matrix shown in Figure 4.5 (b) – (e). These images displayed large agglomerations of um-CNF bundles along with a cavity due to pull-out of um-CNF aggregates, which increased with increase in um-CNF content, indicating poor interfacial adhesion[6,27,157]. This corresponds to the brittle properties and has adverse effect on the mechanical properties of the nanocomposites as observed in Figure 4.6.

The addition of 0.3 and 0.5 wt. % m-CNF into epoxy exhibited slightly rougher and coarser fracture surfaces when compared to neat epoxy (Figure 4.5 (f) and (g)). Furthermore, there were no visible aggregations, voids and pull-outs along the stretching direction observed at this scale for these nanocomposites (especially for 0.5 wt. % m-CNF), signifying improved compatibility with epoxy due to the modified CNF, which resulted in better interfacial adhesion. This also indicates that relatively higher amount of energy was consumed to break these nanocomposites due to the homogenously dispersed m-CNF acting as a hindrance towards the crack propagation causing crack deflection. Consequently, this leads to late breakage or rupture of the nanocomposites, corresponding to an increase in tensile properties. Saba et al. [27] also showed SEM images of bleached CNF/epoxy nanocomposites at low content of 0.5 and 0.75 wt.% CNF, with a good interfacial adhesion between CNFs and epoxy matrix, and no aggregations.

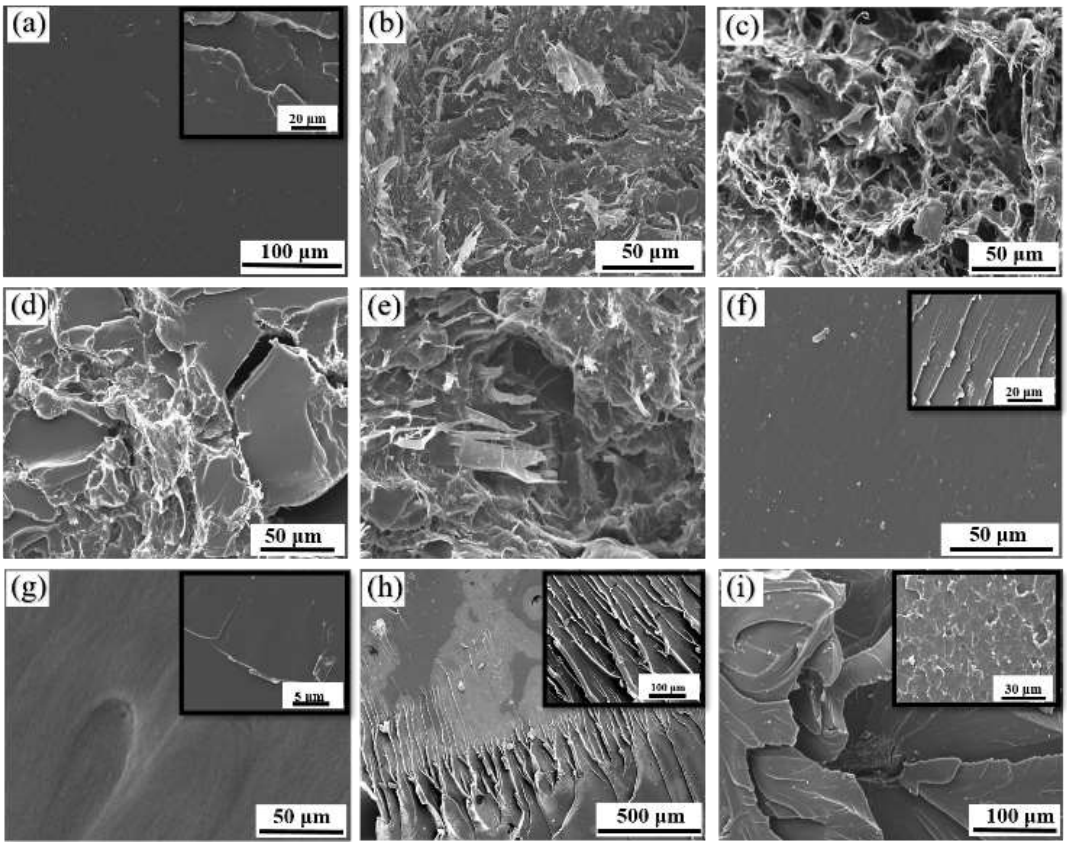

Figure 4.5 SEM images of fracture surface of epoxy nanocomposites with (a) – (e) 0, 0.3, 0.5, 1 and 3 wt.% um-CNF, respectively and (f) – (i) 0.3, 0.5, 1 and 3 wt.% m-CNF, respectively.

At higher concentrations of 1 and 3 wt. % of m-CNF, filler agglomerations and micro-voids were formed in epoxy nanocomposites as evident by Figure 4.5 (h) and (i). Furthermore, at high magnifications, the nanofibrils are discerned as white dots (inset in Figure 4.5 (h) and (i)). These m-CNF aggregations decrease the overall filler-matrix interfacial area, which decreases the potential reinforcing effect of the m-CNFs. Micro-voids and porosity in the nanocomposites act as weak interfaces and create stress concentrations leading to premature failure when applying tensile stress. These defects tend to decrease the mechanical properties (tensile strength and modulus) compared to 0.5 wt.% m-CNF/epoxy nanocomposites. Similar arguments were also reported by Saba et al.[27] and

Lu et al.[157], showing aggregates and voids formation in epoxy nanocomposites as one of the factors, which governs to pre-mature failure during tensile testing.

4.3.3 Comparative mechanical studies of m-CNF and um-CNF/epoxy nanocomposites

The mechanical performance of neat epoxy and its nanocomposites were evaluated with uniaxial tensile testing. Figure 4.6 compared the effects of reinforcing um-CNF and m-CNF at different concentrations on elastic modulus (E), tensile strength (σ_{TS}), work-of-fracture (WOF) and strain-at-failure (SAF) of nanocomposites. It was observed that m-CNF showed better properties than um-CNF when filled in epoxy at the same loading. At 0.3 wt. %, the m-CNF nanocomposite showed an improvement in E, σ_{TS}, and WOF by ~30 % compared to the um-CNF nanocomposite. This trend became more prominent at the higher concentration of 0.5 wt. %, with an increment of ~62%, 35 % and 50 % in E, σ_{TS}, and WOF respectively. Moreover, the 0.3 wt. % m-CNF showed better performance than the 0.5 wt. % um-CNF nanocomposites. Hence, lower content m-CNF is required to achieve a higher mechanical performance than um-CNF and can achieve a higher possible performance, overall. Girouard et al.[21] reported a similar trend, where 1 wt.% modified nanocellulose composite improved σ_{TS} and WOF by ~ 42 % compared to unmodified composite. In fact, 1 wt. % modified samples (σ_{TS}: ~90.5 %; WOF: ~73 %) showed better results than 5 wt. % unmodified material (σ_{TS}: 35 % and WOF: ~15%), indicating greater effect of lower concentration of modified specimen is required to get enhanced properties. Similarly, Barari et al.[158] also showed that silylated CNFs reinforced epoxy nanocomposite outperformed the untreated composites.

Figure 4.6 also showed the effect of different loadings of CNFs on the mechanical properties of nanocomposites with respect to the neat epoxy. The specimens filled with um-CNF showed an increase in E but only at 0.3 wt. % CNF loading, which may be due to the higher modulus of CNF (~80 GPa [28,159]) than that of the epoxy (~3 GPa (this work)). However, at higher contents of um-CNF (i.e., 0.5, 1 and 3 wt. %), the E showed no significant increment and ultimately decreased; the σ_{TS} also decreased at these concentrations. This may be due to poor compatibility between the um-CNFs and epoxy that caused inhomogeneous dispersion forming aggregations of CNF networks in the composites. The WOF and SAF decreased slightly or showed insignificant changes indicating embrittlement of nanocomposites. On the contrary, the epoxy with m-CNF enhanced the E and σ_{TS} along with increasing m-CNF content. In Fig. 5a and b, it was observed that the incorporation of m-CNF at 0.5 wt. % exhibited the highest increment of E and σ_{TS} by 72 % and 45 %, respectively, as compared to the neat epoxy. Statistical analysis also confirms this enhancement in the modulus and strength. This behavior may be due to the stiffening effect of m-CNFs, along with homogenous dispersion of m-CNF and high interfacial interaction of filler-matrix, leading to the effective stress transfer between the m-CNFs and the epoxy matrix. However, at higher m-CNF content of 1 and 3 wt. %, E and σ_{TS} decreased when compared to 0.5 wt.% m-CNF/epoxy nanocomposite. This may be attributed to an increase in the inter-particle interaction or agglomerations between the m-CNFs within the epoxy. These agglomerations decreased the overall filler-matrix interfacial area along with increase in the concentration of m-CNFs, which resulted in formation of micro-voids or pores. This tends to decrease the potential reinforcing effect of m-CNFs, leading to premature failure of the composites, followed by decrease in

modulus and strength. WOF tends to follow the similar trend as E and σ_{TS}, showing a maximum increase by ~65 % for epoxy nanocomposite at 0.5 wt.% m-CNF as compared to the neat epoxy, suggesting higher energy absorption before the failure, whereas, the SAF decreased by the addition of CNFs as shown by Figure 4.6 (d).

The improvement in mechanical properties of m-CNF/epoxy nanocomposite in this study is similar or higher than that reported in previous studies. Saba et al. [27] showed a maximum increase in modulus and strength by 50% and 34%, respectively for epoxy composite at 0.75 wt.% chemically modified CNFs. Lu et al. [6] successfully incorporated silane-treated CNF into epoxy resin and improved the modulus by 25 % at 3.7 wt. % m-CNF, and Zhang et al.[160] showed an increment of 27% and 38% in tensile strength and modulus, respectively, upon addition of only 0.2 wt. % of CNF into epoxy matrix. These results demonstrate that the functionalized CNF is effective at improving the compatibility with the matrix and enhancing the mechanical properties of the resulting nanocomposites as compared to um-CNFs.

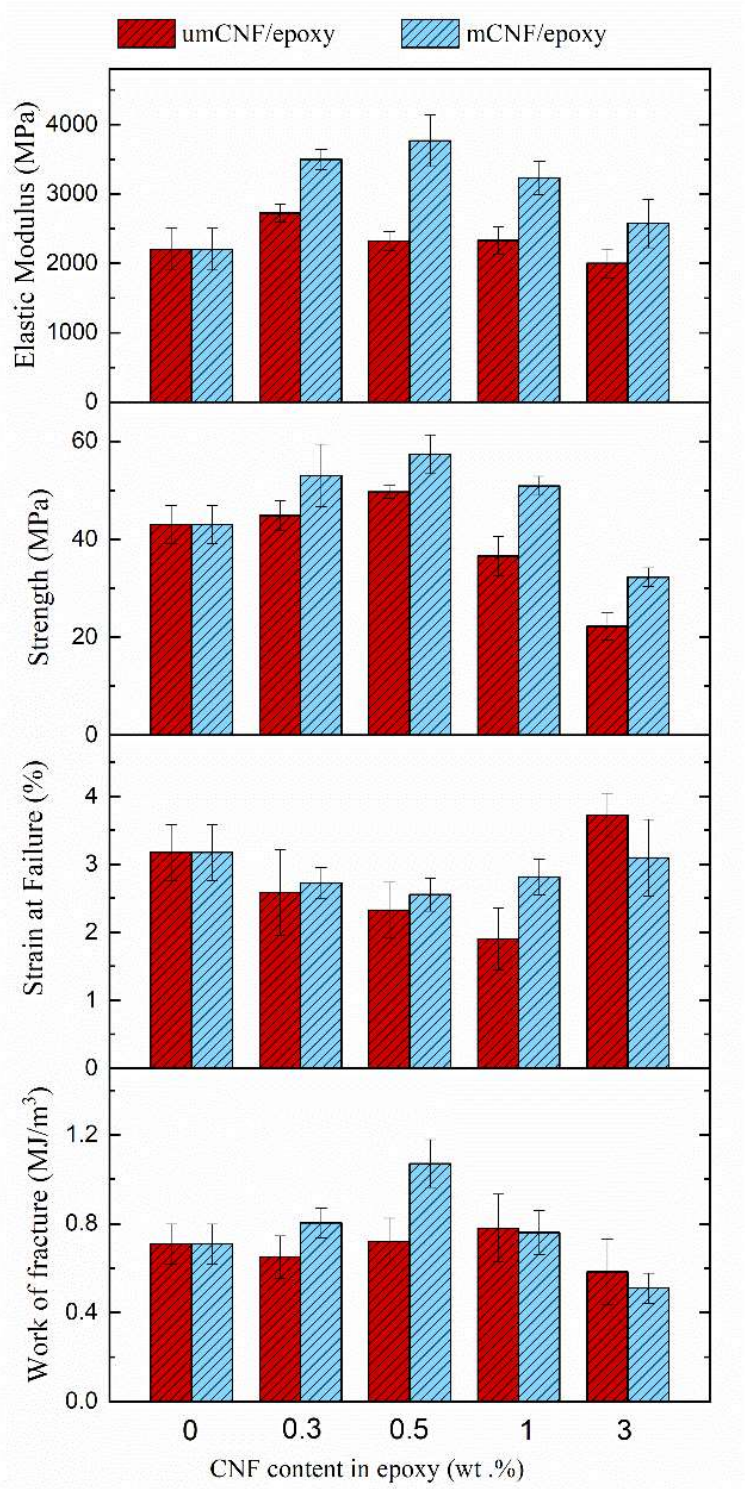

Figure 4.6 Tensile properties of m-CNF and um-CNF reinforced epoxy nanocomposites: (a) elastic modulus, (b) tensile strength, (c) strain at failure, and (d) work of fracture.

From another study, it has been observed that m-CNFs lead to higher composite moduli than the modified cellulose nanocrystals (m-CNCs) at the same filler loading. CNFs form long fiber networks with fibril diameter-like or larger than CNCs [28]. It was reported by Peng et al. [29] that the epoxy with acetylated CNC improved its E and σ_{TS} by ~23 % and ~28%, respectively at 5 wt.% of m-CNC. Whereas in this work, the E and σ_{TS} of the nanocomposites increased by ~60 % and 35%, respectively at only 0.5 wt.% m-CNF. This may be mainly due to the higher aspect ratio and entanglements of m-CNFs assisting in fibril-matrix and fibril-fibril load transfers contributing to the higher moduli [28]. The studies have found that longer fibrils with relatively low strength exhibit stronger reinforcing effect than short high-strength fibers [8,28], indicating that fiber aspect ratio is a very important factor to be considered while choosing fillers for reinforcing composites.

4.3.4 Thermal Properties of CNF/epoxy nanocomposites

Thermal stability of neat epoxy and its nanocomposites was studied using TGA. Weight loss thermograms and derivative curves in Figure 4.7 show two degradation steps for the nanocomposites. The first degradation occurred over the temperature range of 300 - 420 °C. It is evident from the thermograph that the degradation temperature of m-CNF/epoxy increased with the m-CNFs from 0.3 to 0.5 wt.%, while decomposition rate decreased. This indicates that reinforcing m-CNFs leads to relatively higher thermal stability and heat resistibility of highly cross-linked filler with epoxy in the nanocomposites. Similar behaviors are also reported by Lee et al. [161] and Saba et al. [9] for bacterial cellulose and cellulose nanofibers in epoxy, respectively. The final degradation occurred above the temperature 400 °C, which is mainly due to the decomposition of

carbonaceous materials to yield carbon and hydrocarbons and volatiles from the epoxy moieties and residual mass. [27]

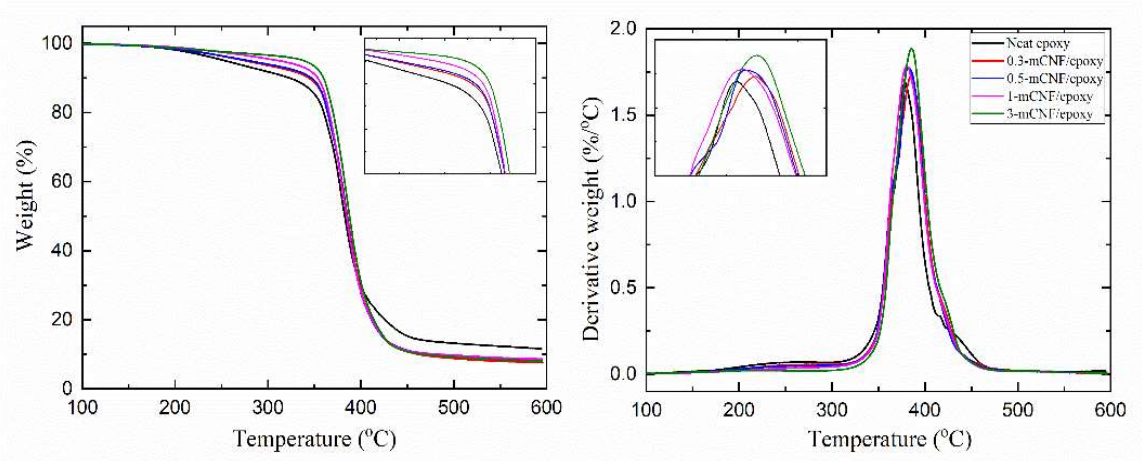

Figure 4.7 (a) TG and (b) DTG curves of CNF/epoxy nanocomposites using TGA.

Figure 4.8 shows T_g values of CNF/epoxy nanocomposites as a function of CNF content. It is evident that m-CNF/epoxy display higher values of T_g as compared to neat epoxy. A significant increase in T_g was observed with 0.3 and 0.5 wt.% m-CNF content and a maximum increase of 5 °C observed at 0.5 wt.% filler loading. The increment in T_g indicates that the inclusion of m-CNF to the epoxy acted as a hindrance and restricted the chain segmental motion of the epoxy cross-linked network either through physical or chemical interactions. Previous work by Saba et al. [9] and Xu et al. [162] also reported the similar trend for epoxy composites containing CNCs. um-CNF filled nanocomposites did not show significant changes in T_g and decreased slightly when compared to neat epoxy. This may be due to lack of proper interaction between filler-matrix and filler particles creating free-volume readily [29,148].

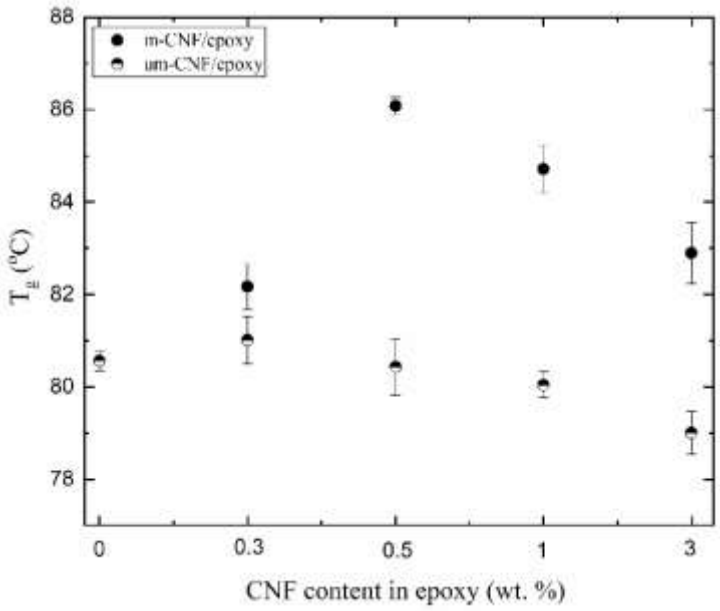

Figure 4.8 T_g of neat epoxy and CNF/epoxy nanocomposites determined from DSC data.

4.4 **Conclusions**

Epoxy nanocomposites with um/m-CNFs were fabricated at different filler concentrations and performance-based comparative analysis was conducted. m-CNFs showed better dispersion in cured epoxy than um-CNFs leading to agglomerations. Epoxy with m-CNF also showed better mechanical properties than the um-CNF at the same loading. Tensile strength, elastic modulus, and work-of-fracture greatly improved with increasing m-CNF content up to 0.5 wt.%, indicating good reinforcement. After this, the properties plateaued and eventually decreased, possibly due to the loss in CNF dispersion at higher loading. um-CNF did not have significant effects on the mechanical properties of epoxy, probably due to incompatibility and lack of interfacial adhesion between filler and matrix. m-CNFs also showed higher thermal stability with epoxy and the value of T_g also increased up to 5 °C, unlike um-CNFs that have insignificant or negative effect. Overall, this study suggests that surface modification of TOCNF provides higher reinforcement

effect with enhanced final properties of nanocomposites even at low filler content when compared to other cellulose-based fillers [29,157,162]. These outstanding properties are likely due to high aspect ratio, better dispersion and distribution of nanofibrils in epoxy. Therefore, water-based surface modified TOCNF can be used as new nanofillers to design renewable nanocomposites with improved properties.

CHAPTER 5. CONCLUSIONS AND FUTURE WORK

Here, we explored the structural control, processing and property relationship of CNCs and CNFs with thermoplastics and thermosets for the enhancement of hygroscopic, mechanical, thermal and optical properties in nanocomposites. The in-plane coefficient of hygroscopic swelling of self-organized and shear-oriented CNC films were highly dependent on the alignment of the nanocrystals within the films. The films with high CNC alignment showed dramatically reduced hygroscopic expansion than those reported for other cellulosic material such as wood, or commonly used polymer thin films, such as polyimide. These films are highly crystalline with a reduced number of hydroxyl groups accessible to water molecules leading to a lower capacity of water sorption and expansion. Due to the induced anisotropy, the CHS of CNC films in the direction perpendicular to shear alignment was higher than the commonly used engineering polymers. Furthermore, finite element analysis (FEA) simulation suggested moisture diffusion as the sole mechanism causing hygroscopic swelling in the CNC films.

CNCs derived from wood pulp and cotton fibers (with different aspect ratio) were used as fillers to produce continuous CNC-reinforced PVA composite fibers by using dry-jet-wet spinning, which is a feasible technique for development of high content aligned CNC. Elastic modulus and tensile strength of the fibers improved significantly by adding CNC up to 15 wt. %, after which the properties plateaued or decreased, possibly due to defects formation from a loss in CNC dispersion or residual pores. Strain-to-failure of the fibers decreased with the addition of CNCs, however, the flexibility of the fibers remained intact. Furthermore, the mechanical properties of fibers filled with cotton CNC were higher than those with wood CNC at the same amount of CNCs due to their longer length or higher

aspect ratio that have outsized effect owing to the structural arrangement of the CNC in the polymer. The drawn fibers also exhibited highly oriented CNC with excellent mechanical performances. Micromechanical models suggest that the increase in elastic modulus of PVA-CNC continuous fiber resulted from high interfacial adhesion between CNC and PVA, increased orientation parameter and CNC concentration, and greater aspect ratio and that the CNCs observed shear-lag behavior.

In order to investigate effects of CNFs on the properties of epoxy, nanocomposites with um/m-CNFs were fabricated with varying filler contents. The hydroxyl groups of CNFs have been functionalized via chemical reactions to change the surface chemistry of CNFs using a water-based method. This method increased the interfacial compatibility of CNFs and epoxy resin along with better dispersion leading to high strength and stiff epoxy. Tensile strength, elastic modulus, and work-of-fracture greatly improved with increasing m-CNF content up to 0.5 wt.%, indicating good reinforcement. um-CNF did not have significant effects on the mechanical properties of epoxy, probably due to incompatibility and lack of interfacial adhesion between filler and matrix. m-CNFs also showed higher thermal stability with epoxy. The outstanding properties of m-CNF/epoxy are likely due to high aspect ratio, better dispersion and distribution of nanofibrils in epoxy. Also, the water-based surface modified TOCNF can be used as new nanofillers to design renewable nanocomposites with improved properties and various polymer matrices in the future.

REFERENCES

(1) Benmokrane, B.; Elgabbas, F.; Ahmed, E. A.; Cousin, P. Characterization and Comparative Durability Study of Glass/Vinylester, Basalt/Vinylester, and Basalt/Epoxy FRP Bars. *J. Compos. Constr.* **2015**, *19* (6), 04015008.

(2) Rodriguez, N. M. A Review of Catalytically Grown Carbon Nanofibers. *J. Mater. Res.* **1993**, *8* (12), 3233–3250.

(3) Al-Saleh, M. H.; Sundararaj, U. Electromagnetic Interference Shielding Mechanisms of CNT/Polymer Composites. *Carbon N. Y.* **2009**, *47* (7), 1738–1746.

(4) Masuelli, M. A. Introduction of Fibre-Reinforced Polymers − Polymers and Composites : Concepts , Properties and Processes. *Technol. Appl. Concr. Repair* **2013**, 3–40.

(5) Fujisawa, S.; Ikeuchi, T.; Takeuchi, M.; Saito, T.; Isogai, A. Superior Reinforcement Effect of TEMPO-Oxidized Cellulose Nanofibrils in Polystyrene Matrix: Optical, Thermal, and Mechanical Studies. *Biomacromolecules* **2012**, No. 13, 2188–2194.

(6) Lu, J.; Askeland, P.; Drzal, L. T. Surface Modification of Microfibrillated Cellulose for Epoxy Composite Applications. *Polymer (Guildf).* **2008**, *49* (5), 1285–1296.

(7) Holbery, J.; Houston, D. Natural-Fiber-Reinforced Polymer Composites in Automotive Applications. *Jom* **2006**, *58* (11), 80–86.

(8) Moon, R. J.; Martini, A.; Nairn, J.; Simonsen, J.; Youngblood, J. Cellulose Nanomaterials Review: Structure, Properties and Nanocomposites. *Chem. Soc. Rev.* **2011**, *40*, 3941.

(9) Saba, N.; Safwan, A.; Sanyang, M. L.; Mohammad, F.; Pervaiz, M.; Jawaid, M.; Alothman, O. Y.; Sain, M. Thermal and Dynamic Mechanical Properties of Cellulose Nanofibers Reinforced Epoxy Composites. *Int. J. Biol. Macromol.* **2017**, *102*, 822–828.

(10) Habibi, Y. Key Advances in the Chemical Modification of Nanocelluloses. *Chem. Soc. Rev.* **2014**, *43* (5), 1519–1542.

(11) Azizi Samir, M. A. S.; Alloin, F.; Dufresne, A. Review of Recent Research into Cellulosic Whiskers, Their Properties and Their Application in Nanocomposite Field. *Biomacromolecules* **2005**, *6*, 612–626.

(12) Dufresne, A. Processing of Polymer Nanocomposites Reinforced with Polysaccharide Nanocrystals. *Molecules* **2010**, *15*, 4111–4128.

(13) Qing, Y.; Wu, Y.; Cai, Z.; Li, X. Water-Triggered Dimensional Swelling of Cellulose Nanofibril Films: Instant Observation Using Optical Microscope. *J. Nanomater.* **2013**, *2013*, 1–6.

(14) Park, S.; Baker, J. O.; Himmel, M. E.; Parilla, P. A.; Johnson, D. K. Cellulose Crystallinity Index: Measurement Techniques and Their Impact on Interpreting Cellulase Performance. *Biotechnol. Biofuels* **2010**, *3*, 10.

(15) Elazzouzi-Hafraoui, S.; Nishiyama, Y.; Putaux, J.-L.; Heux, L.; Dubreuil, F.; Rochas, C. The Shape and Size Distribution of Crystalline Nanoparticles Prepared by Acid Hydrolysis of Native Cellulose. *Biomacromolecules* **2008**, *9*, 57–65.

(16) Moon, R. J.; Martini, A.; Nairn, J.; Simonsen, J.; Youngblood, J. Cellulose Nanomaterials Review: Structure, Properties and Nanocomposites. *Chem. Soc. Rev.* **2011**, *40*, 3941.

(17) Lahiji, R. R.; Xu, X.; Reifenberger, R.; Raman, A.; Rudie, A.; Moon, R. J. Atomic Force Microscopy Characterization of Cellulose Nanocrystals. *Langmuir* **2010**, *26*,

(18) Shrestha, S.; Montes, F.; Schueneman, G. T.; Snyder, J. F.; Youngblood, J. P. Effects of Aspect Ratio and Crystal Orientation of Cellulose Nanocrystals on Properties of Poly(Vinyl Alcohol) Composite Fibers. *Compos. Sci. Technol.* **2018**, *167* (August), 482–488.

(19) Clarkson, C. M.; Youngblood, J. P. Dry-Spinning of Cellulose Nanocrystal/Polylactic Acid Composite Fibers. *Green Mater.* **2018**, 1–33.

(20) Peng, S. X.; Shrestha, S.; Yoo, Y.; Youngblood, J. P. Enhanced Dispersion and Properties of a Two-Component Epoxy Nanocomposite Using Surface Modified Cellulose Nanocrystals. *Polymer (Guildf).* **2017**, *112*, 359–368.

(21) Girouard, N. M.; Xu, S.; Schueneman, G. T.; Shofner, M. L.; Meredith, J. C. Site-Selective Modification of Cellulose Nanocrystals with Isophorone Diisocyanate and Formation of Polyurethane-CNC Composites. *ACS Appl. Mater. Interfaces* **2016**, *8* (2), 1458–1467.

(22) Liu, J.-C.; Moon, R. J.; Rudie, A.; Youngblood, J. P. Mechanical Performance of Cellulose Nanofibril Film-Wood Flake Laminate. *Holzforschung* **2014**, *68* (3).

(23) Iwamoto, S.; Nakagaito, A. N.; Yano, H. Nano-Fibrillation of Pulp Fibers for the Processing of Transparent Nanocomposites. *Appl. Phys. A* **2007**, *89* (2), 461–466.

(24) Zimmermann, T.; Pöhler, E.; Geiger, T. Cellulose Fibrils for Polymer Reinforcement. *Adv. Eng. Mater.* **2004**, *6*, 754–761.

(25) Kalia, S.; Dufresne, A.; Cherian, B. M.; Kaith, B. S.; Avérous, L.; Njuguna, J.; Nassiopoulos, E. Cellulose-Based Bio- and Nanocomposites: A Review. *Int. J. Polym. Sci.* **2011**, *2011*.

(26) Lee, W. J.; Clancy, A. J.; Kontturi, E.; Bismarck, A.; Shaffer, M. S. P. Strong and Stiff: High-Performance Cellulose Nanocrystal/Poly(Vinyl Alcohol) Composite Fibers. *ACS Appl. Mater. Interfaces* **2016**, *8* (46), 31500–31504.

(27) Saba, N.; Mohammad, F.; Pervaiz, M.; Jawaid, M.; Alothman, O. Y.; Sain, M. Mechanical, Morphological and Structural Properties of Cellulose Nanofibers Reinforced Epoxy Composites. *Int. J. Biol. Macromol.* **2017**, *97*, 190–200.

(28) Xu, X.; Liu, F.; Jiang, L.; Zhu, J. Y.; Haagenson, D.; Wiesenborn, D. P. Cellulose Nanocrystals vs. Cellulose Nanofibrils: A Comparative Study on Their Microstructures and Effects as Polymer Reinforcing Agents. *ACS Appl. Mater. Interfaces* **2013**, *5* (8), 2999–3009.

(29) Peng, S. X.; Shrestha, S.; Yoo, Y.; Youngblood, J. P. Enhanced Dispersion and Properties of a Two-Component Epoxy Nanocomposite Using Surface Modified Cellulose Nanocrystals. *Polym. (United Kingdom)* **2017**, *112*, 359–368.

(30) Agrawal, A. M.; Manek, R. V.; Kolling, W. M.; Neau, S. H. Water Distribution Studies within Microcrystalline Cellulose and Chitosan Using Differential Scanning Calorimetry and Dynamic Vapor Sorption Analysis. *J. Pharm. Sci.* **2004**, *93*, 1766–1779.

(31) Ardebili, H.; Wong, E. H.; Pecht, M. Hygroscopic Swelling and Sorption Characteristics of Epoxy Molding Compounds Used in Electronic Packaging. *IEEE Trans. Components Packag. Technol.* **2003**, *26* (1), 206–214.

(32) Koh, S. W.; Lim, T. B. The Mechanics and Impact of Hygroscopic Swelling of Polymeric Materials. **2013**, *124* (June 2002), 122–126.

(33) Yao, L.; Haas, T. W.; Guiseppi-Elie, A.; Bowlin, G. L.; Simpson, D. G.; Wnek, G. E. Electrospinning and Stabilization of Fully Hydrolyzed Poly(Vinyl Alcohol) Fibers. *Chem. Mater.* **2003**, *15*, 1860–1864.

(34) Kenawy, E.-R.; Bowlin, G. L.; Mansfield, K.; Layman, J.; Simpson, D. G.; Sanders, E. H.; Wnek, G. E. Release of Tetracycline Hydrochloride from Electrospun Poly(Ethylene-Co-Vinylacetate), Poly(Lactic Acid), and a Blend. *J. Control. Release* **2002**, *81*, 57–64.

(35) Peresin, M. S.; Habibi, Y.; Zoppe, J. O.; Pawlak, J. J.; Rojas, O. J. Nanofiber Composites of Polyvinyl Alcohol and Cellulose Nanocrystals: Manufacture and Characterization. *Biomacromolecules* **2010**, *11*, 674–681.

(36) Koski, A.; Yim, K.; Shivkumar, S. Effect of Molecular Weight on Fibrous PVA Produced by Electrospinning. *Mater. Lett.* **2004**, *58*, 493–497.

(37) Yuwawech, K.; Wootthikanokkhan, J.; Tanpichai, S. Effects of Two Different Cellulose Nanofiber Types on Properties of Poly(Vinyl Alcohol) Composite Films. *J. Nanomater.* **2015**, *2015*, 1–10.

(38) Nakagaito, A. N.; Yano, H. The Effect of Fiber Content on the Mechanical and Thermal Expansion Properties of Biocomposites Based on Microfibrillated Cellulose. *Cellulose* **2008**, *15*, 555–559.

(39) Wang, C. Y.; Fuentes-Hernandez, C.; Liu, J. C.; Dindar, A.; Choi, S.; Youngblood, J. P.; Moon, R. J.; Kippelen, B. Stable Low-Voltage Operation Top-Gate Organic Field-Effect Transistors on Cellulose Nanocrystal Substrates. *ACS Appl. Mater. Interfaces* **2015**, *7*, 4804–4808.

(40) Zhou, Y.; Khan, T. M.; Liu, J. C.; Fuentes-Hernandez, C.; Shim, J. W.; Najafabadi, E.; Youngblood, J. P.; Moon, R. J.; Kippelen, B. Efficient Recyclable Organic Solar Cells on Cellulose Nanocrystal Substrates with a Conducting Polymer Top Electrode Deposited by Film-Transfer Lamination. *Org. Electron. physics, Mater. Appl.* **2014**, *15*, 661–666.

(41) Diaz, J. A.; Wu, X.; Martini, A.; Youngblood, J. P.; Moon, R. J. Thermal Expansion of Self-Organized and Shear-Oriented Cellulose Nanocrystal Films. *Biomacromolecules* **2013**, *14*, 2900–2908.

(42) Niinivaara, E.; Faustini, M.; Tammelin, T.; Kontturi, E. Water Vapor Uptake of Ultrathin Films of Biologically Derived Nanocrystals: Quantitative Assessment with Quartz Crystal Microbalance and Spectroscopic Ellipsometry. *Langmuir* **2015**, *31*, 12170–12176.

(43) Mariano, M.; El Kissi, N.; Dufresne, A. Cellulose Nanocrystals and Related Nanocomposites: Review of Some Properties and Challenges. *J. Polym. Sci. Part B Polym. Phys.* **2014**, *52*, 791–806.

(44) Aulin, C.; Ahola, S.; Josefsson, P.; Nishino, T.; Hirose, Y.; Österberg, M.; Wågberg, L. Nanoscale Cellulose Films with Different Crystallinities and Mesostructures—Their Surface Properties and Interaction with Water. *Langmuir* **2009**, *25*, 7675–7685.

(45) Diaz, J. A.; Ye, Z.; Wu, X.; Moore, A. L.; Moon, R. J.; Martini, A.; Boday, D. J.; Youngblood, J. P. Thermal Conductivity in Nanostructured Films: From Single Cellulose Nanocrystals to Bulk Films. *Biomacromolecules* **2014**, *15*, 4096–4101.

(46) Agrawal, A. M.; Manek, R. V.; Kolling, W. M.; Neau, S. H. Studies on the Interaction of Water with Ethylcellulose: Effect of Polymer Particle Size. *AAPS PharmSciTech* **2003**, *4*, 469–479.

(47) Stellrecht, E.; Han, B.; Pecht, M. Measurement of the Hygroscpic Swelling. In *Experimental Techniques*; 2003; pp 40–44.

(48) Fält, S.; Wågberg, L.; Vesterlind, E.-L. Swelling of Model Films of Cellulose Having Different Charge Densities and Comparison to the Swelling Behavior of Corresponding Fibers. *Langmuir* **2003**, *19*, 7895–7903.

(49) Ahola, S.; Salmi, J.; Johansson, L.-S.; Laine, J.; Österberg, M. Model Films from Native Cellulose Nanofibrils. Preparation, Swelling, and Surface Interactions. *Biomacromolecules* **2008**, *9*, 1273–1282.

(50) Josefsson, P.; Henriksson, G.; Wågberg, L. The Physical Action of Cellulases Revealed by a Quartz Crystal Microbalance Study Using Ultrathin Cellulose Films and Pure Cellulases. *Biomacromolecules* **2008**, *9*, 249–254.

(51) El-Sa'ad, L.; Darby, M. I.; Yates, B. Moisture Absorption by Epoxy Resins: The Reverse Thermal Effect. *J. Mater. Sci.* **1990**, *25*, 3577–3582.

(52) Buchhold, R.; Nakladal, A.; Gerlach, G.; Sahre, K.; Eichhorn, K.-J.; Herold, M.; Gauglitz, G. Influence of Moisture-Uptake on Mechanical Properties of Polymers Used in Microelectronics. *MRS Proc.* **1998**, *511*, 359.

(53) Diaz, J. A.; Moon, R. J.; Youngblood, J. P. Contrast Enhanced Microscopy Digital Image Correlation: A General Method to Contact-Free Coefficient of Thermal Expansion Measurement of Polymer Films. *ACS Appl. Mater. Interfaces* **2014**, *6*, 4856–4863.

(54) de Boer, J. *The Dynamic Character of Adsorption*, 2nd ed.; Clarendon Prress: London, UK, 1968.

(55) Guggenheim, E. A. *Appilcations of Statistical Mechanics*; Clarendon Press: Oxford, UK, 1966.

(56) Andrade, R. D.; Lemus, R.; Perez, C. E. Models of Sorption Isotherms for Food: Uses and Limitations. *Vitae-Revista La Fac. Quim. Farm.* **2011**, *18*, 324–333.

(57) Kohler, R.; Dück, R.; Ausperger, B.; Alex, R. A Numeric Model for the Kinetics of Water Vapor Sorption on Cellulosic Reinforcement Fibers. *Compos. Interfaces* **2003**, *10*, 255–276.

(58) Xie, Y.; Hill, C. A. S. Kinetic Water Vapour Sorption of Sitka Spruce at Variable Temperature Using the Parallel Exponential Kinetics Model. *Int. Res. Gr. Wood Perservation* **2010**, 4–7.

(59) Reiner, R. S.; Rudie, A. W. Process Scale-Up of Cellulose Nanocrystal Production to 25 Kg per Batch at the Forest Products Laboratory. *Prod. Appl. Cellul. Nanomater.* **2013**, 21–24.

(60) Reising, A. B.; Moon, R. J.; Youngblood, J. P. Effect of Particle Alignment on Mechanical Properties of Neat Cellulose Nanocrystal Films. *J. Sci. Technol. For. Prod. Process.* **2013**, *2*, 32–41.

(61) Park, S. B.; Dhakal, R.; Joshi, R. Comparative Analysis of BGA Deformations and Strains Using Digital Image Correlation and Moire Interferometry. In *Proceeding of the Society for Experimental Mechanics*; Portland, OR, USA, 2005; pp 1–8.

(62) Sutton, M. A.; McNeill, S. R.; Helm, J. D.; Chao, Y. J. Advances in Two-Dimensional and Three-Dimensional Computer Vision. In *Photomechanics*; Springer Berlin Heidelberg: Berlin, Heidelberg; pp 323–372.

(63) Thompson, R.; Hemker, K. No Title. *Proc. SEM Conf. Exp. Mech.* **2007**, *2*, 1058–1067.

(64) Topgaard, D.; Söderman, O. Diffusion of Water Absorbed in Cellulose Fibers Studied with 1 H-NMR. *Langmuir* **2001**, *17*, 2694–2702.

(65) Sung Yi; Jing Sua Goh; Ji Cheng Yang. Residual Stresses in Plastic IC Packages during Surface Mounting Process Preceded by Moisture Soaking Test. *IEEE Trans. Components, Packag. Manuf. Technol. Part B* **1997**, *20*, 247–255.

(66) Pyo, J.-B.; Lee, T.-I.; Kim, C.; Kim, M. S.; Kim, T.-S. Prediction of Time-Dependent Swelling of Flexible Polymer Substrates Using Hygro-Mechanical Finite Element Simulations. *Soft Matter* **2016**, *12*, 4135–4141.

(67) Wolff, E. G. Moisture Induced Dimensional Changes in Composites. In *Proceedings 13th International Conference on Composite Materials (ICCM/13)*; Beijing, China, 2001.

(68) Gamstedt, E. K. Moisture Induced Softening and Swelling of Natural Cellulose Fibres in Composite Applications. *IOP Conf. Ser. Mater. Sci. Eng.* **2016**, *139*, 012003.

(69) Shirangi, M. H.; Michel, B. Mechanism of Moisture Diffusion, Hygroscopic Swelling, and Adhesion Degradation in Epoxy Molding Compounds. *Moisture Sensit. Plast. Packag. IC Devices* **2010**, 29–69.

(70) Stellrecht, E.; Han, B.; Pecht, M. G. Characterization of Hygroscopic Swelling Behavior of Mold Compounds and Plastic Packages. *IEEE Trans. Components Packag. Technol.* **2004**, *27*, 499–506.

(71) Fan, X. J.; Lee, S. W. R.; Han, Q. Experimental Investigations and Model Study of Moisture Behaviors in Polymeric Materials. *Microelectron. Reliab.* **2009**, *49*, 861–871.

(72) Skaar, C. Hygroexpansion in Wood. In *Wood-Water Relations*; Springer Berlin Heidelberg, 1988; pp 122–176.

(73) Young, J. H.; Nelson, G. L. Research of Hysteresis Between Sorption and Desorption Isotherms of Wheat. *Trans ASAE* **1967**, *10*, 756–761.

(74) York, P. Analysis of Moisture Sorption Hysteresis in Hard Gelatin Capsules, Maize Starch, and Maize Starch: Drug Powder Mixtures. *J. Pharm. Pharmacol.* **1981**, *33*, 269–273.

(75) Locke, E. G. Wood and Cellulose Science. Alfred J. Stamm. Ronald. *Sci. AAAS* **1965**, *147*, 595–596.

(76) Zografi, G.; Kontny, M. J.; Yang, A. Y. S.; Brenner, G. S. Surface Area and Water Vapor Sorption of Microcrystalline Cellulose. *Int. J. Pharm.* **1984**, *18*, 99–116.

(77) Sadeghnejad, G. R.; York, P.; Stanley-Wood, N. G. Water Vapour Interaction with Pharmaceutical Cellulose Powders. *Drug Dev. Ind. Pharm.* **1986**, *12*, 2171–2192.

(78) Khan, F.; Pilpel, N. An Investigation of Moisture Sorption in Microcrystalline Cellulose Using Sorption Isotherms and Dielectric Response. *Powder Technol.* **1987**, *50*, 237–241.

(79) Zografi, G.; Kontny, M. J. The Intearctions of Water Cellulose- and Starch-Derived Pharmaceutical Excipients. *Pharm. Res.* **1986**, *3*, 187–194.

(80) Gocho, H. Effect of Polymer Chain End on Sorption Isotherm of Water by Chitosan. *Carbohydr. Polym.* **2000**, *41*, 87–90.

(81) Hollenbeck, R. G.; Peck, G. E.; Kildsig, D. O. Application of Immersional Calorimetry to Investigation of Solid-Liquid Interactions: Microcrystalline Cellulose-Water System. *J. Pharm. Sci.* **1978**, *67*, 1599–1606.

(82) Maroulis, Z. B.; Tsami, E.; Marinos-Kouris, D.; Saravacos, G. D. Application of the GAB Model to the Moisture Sorption Isotherms for Dried Fruits. *J. Food Eng.* **1988**, *7*, 63–78.

(83) Yoo, Y.; Youngblood, J. P. Green One-Pot Synthesis of Surface Hydrophobized Cellulose Nanocrystals in Aqueous Medium. *ACS Sustain. Chem. Eng.* **2016**, *4*, 3927–3938.

(84) Nakao, Y.; Fukuoka, E.; Nakajima, S.; Hasegawa, J. Crystallinity and Physical Characteristics of Microcrystalline Cellulose. *Chem. Pharm. Bull. (Tokyo).* **1977**, *25*, 96–101.

(85) Belbekhouche, S.; Bras, J.; Siqueira, G.; Chappey, C.; Lebrun, L.; Khelifi, B.; Marais, S.; Dufresne, A. Water Sorption Behavior and Gas Barrier Properties of Cellulose Whiskers and Microfibrils Films. *Carbohydr. Polym.* **2011**, *83*, 1740–1748.

(86) Okubayashi, S.; Bechtold, T. Alkali Uptake and Swelling Behavior of Lyocell Fiber and Their Effects on Crosslinking Reaction. *Cellulose* **2005**, *12*, 459–467.

(87) Kim, Y.; Liu, D.; Lee, H.; Liu, R.; Sengupta, D.; Park, S. Investigation of Stress in MEMS Sensor Device Due to Hygroscopic and Viscoelastic Behavior of Molding Compound. *IEEE Trans. Components, Packag. Manuf. Technol.* **2015**, *5*, 945–955.

(88) Rafsanjani, A.; Stiefel, M.; Jefimovs, K.; Mokso, R.; Derome, D.; Carmeliet, J. Hygroscopic Swelling and Shrinkage of Latewood Cell Wall Micropillars Reveal Ultrastructural Anisotropy. *J. R. Soc. Interface* **2014**, *11*, 20140126.

(89) Patera, A.; Derome, D.; Griffa, M.; Carmeliet, J. Hysteresis in Swelling and in Sorption of Wood Tissue. *J. Struct. Biol.* **2013**, *182*, 226–234.

(90) Jang, C.; Yoon, S.; Han, B. Measurement of the Hygroscopic Swelling Coefficient of Thin Film Polymers Used in Semiconductor Packaging. *IEEE Trans. Components Packag. Technol.* **2010**, *33*, 340–346.

(91) Siqueira, G.; Bras, J.; Dufresne, A. Cellulose Whiskers versus Microfibrils: Influence of the Nature of the Nanoparticle and Its Surface Functionalization on the Thermal and Mechanical Properties of Nanocomposites. *Biomacromolecules* **2009**, *10*, 425–432.

(92) Bledzki, A. Composites Reinforced with Cellulose Based Fibres. *Prog. Polym. Sci.* **1999**, *24*, 221–274.

(93) Shrestha, S.; Diaz, J. A.; Ghanbari, S.; Youngblood, J. P. Hygroscopic Swelling Determination of Cellulose Nanocrystal (CNC) Films by Polarized Light Microscopy Digital Image Correlation. *Biomacromolecules* **2017**, *18*, 1482–1490.

(94) Habibi, Y.; Lucia, L. A.; Rojas, O. J. Cellulose Nanocrystals: Chemistry, Self-Assembly, and Applications. *Chem. Rev.* **2010**, *110*, 3479–3500.

(95) Chen, S.; Schueneman, G.; Pipes, R. B.; Youngblood, J.; Moon, R. J. Effects of Crystal Orientation on Cellulose Nanocrystals–Cellulose Acetate Nanocomposite Fibers Prepared by Dry Spinning. *Biomacromolecules* **2014**, *15*, 3827–3835.

(96) Dri, F. L.; Hector, L. G.; Moon, R. J.; Zavattieri, P. D. Anisotropy of the Elastic Properties of Crystalline Cellulose Iβ from First Principles Density Functional Theory with Van Der Waals Interactions. *Cellulose* **2013**, *20*, 2703–2718.

(97) Lee, W. J.; Clancy, A. J.; Kontturi, E.; Bismarck, A.; Shaffer, M. S. P. Strong and Stiff: High-Performance Cellulose Nanocrystal/Poly(Vinyl Alcohol) Composite Fibers. *ACS Appl. Mater. Interfaces* **2016**, *8*, 31500–31504.

(98) Tan, B.; Ching, Y.; Poh, S.; Abdullah, L.; Gan, S. A Review of Natural Fiber Reinforced Poly(Vinyl Alcohol) Based Composites: Application and Opportunity. *Polymers (Basel).* **2015**, *7*, 2205–2222.

(99) Ramezani Kakroodi, A.; Cheng, S.; Sain, M.; Asiri, A. Mechanical, Thermal, and Morphological Properties of Nanocomposites Based on Polyvinyl Alcohol and Cellulose Nanofiber from Aloe Vera Rind. *J. Nanomater.* **2014**, *2014*, 1–7.

(100) Peng, J.; Ellingham, T.; Sabo, R.; Turng, L.-S.; Clemons, C. M. Short Cellulose Nanofibrils as Reinforcement in Polyvinyl Alcohol Fiber. *Cellulose* **2014**, *21*, 4287–4298.

(101) Favier, V.; Chanzy, H.; Cavaillé, J. Y. Polymer Nanocomposites Reinforced by Cellulose Whiskers. *Macromolecules* **1995**, *28*, 6365–6367.

(102) Jalal Uddin, A.; Araki, J.; Gotoh, Y. Toward "Strong" Green Nanocomposites: Polyvinyl Alcohol Reinforced with Extremely Oriented Cellulose Whiskers. *Biomacromolecules* **2011**, *12*, 617–624.

(103) Peresin, M.; Habibi, Y.; Zoppe, J.; Pawlak, J.; Rojas, O. Nanofiber Composites of Polyvinyl Alcohol and Cellulose Nanocrystals: Manufacture and Characterisation. *Biomacromolecules* **2010**, *11*, 674–681.

(104) Clemons, C. Nanocellulose in Spun Continuous Fibers: A Review and Future Outlook. *J. Renew. Mater.* **2016**, *4*, 327–339.

(105) Gabara, V.; Hartzler, J. D.; Lee, K. S. Aramid Fibers. In *Handbook of Fiber Chemistry*; Lewin, M., Ed.; New York: Taylor & Francis: Boca Raton, FL, 2007; pp 1006–1007.

(106) Yasuda, H.; Ban, K.; Ohta, Y. *Gel Spinning Processes*; Woodhead Publishing Limited, 1994.

(107) Reid, M. S.; Villalobos, M.; Cranston, E. D. Benchmarking Cellulose Nanocrystals: From the Laboratory to Industrial Production. *Langmuir* **2017**, 1583–1598.

(108) Salyer, I. O.; Heyd, J. W.; Brodbeck, R. M.; Hartzel, L. W.; Brown, L. E. Use of a Capillary Extrusion Rheometer to Measure Curing of Thermosetting Plastics and Rubbers. *J. Polym. Sci. Part A Gen. Pap.* **1965**, *3*, 1911–1939.

(109) Nishiyama, Y.; Langan, P.; Chanzy, H. Crystal Structure and Hydrogen-Bonding System in Cellulose Iβ from Synchrotron X-Ray and Neutron Fiber Diffraction. *J. Am. Chem. Soc.* **2002**, *124*, 9074–9082.

(110) Uddin, A. J.; Fujie, M.; Sembo, S.; Gotoh, Y. Outstanding Reinforcing Effect of Highly Oriented Chitin Whiskers in PVA Nanocomposites. *Carbohydr. Polym.* **2012**, *87*, 799–805.

(111) Cho, J. D.; Lyoo, W. S.; Chvalun, S. N.; Blackwell, J. X-Ray Analysis and Molecular Modeling of Poly(Vinyl Alcohol)s with Different Stereoregularities. *Macromolecules* **1999**, *32*, 6236–6241.

(112) Peppas, N. A.; Merrill, E. W. Poly(Vinyl Alcohol) Hydrogels: Reinforcement of Radiation-Crosslinked Networks by Crystallization. *J. Polym. Sci. Polym. Chem. Ed.* **1976**, *14*, 441–457.

(113) Halpin, J. C.; Tsai, S. W. *Effects of Environmental Factors on Composite Materials*; 1969.

(114) Helbert, W.; Cavaille, J. Y.; Dufresne, A.; Fourier, U. J. Thermoplastic Nanocomposites Filled With Straw Cellulose Whiskers . Part I : Processing and Mechanical Behavior. *Polym. Compos.* **1996**, *17*, 604–611.

(115) Cox, H. L. The Elasticity and Strength of Paper and Other Fibrous Materials. *Br. J. Appl. Phys.* **1952**, *3*, 72–79.

(116) Krenchel, H. *Fibre Reinforcement*; Akademisk Forlag: Copenhagen, Denmark, 1964.

(117) Coleman, J. N.; Cadek, M.; Blake, R.; Nicolosi, V.; Ryan, K. P.; Belton, C.; Fonseca, A.; Nagy, J. B.; Gun'ko, Y. K.; Blau, W. J. High Performance Nanotube-Reinforced Plastics: Understanding the Mechanism of Strength Increase. *Adv. Funct. Mater.* **2004**, *14*, 791–798.

(118) Landel, R. F.; Nielsen, L. E. Mechanical Properties of Polymers and Composites. In *Mechanical Properties of Polymers and Composites*; Marcel Dekker: New York, 1974; p 380.

(119) Revol, J.-F.; Godbout, L.; Dong, X.-M.; Gray, D. G.; Chanzy, H.; Maret, G. Chiral Nematic Suspensions of Cellulose Crystallites; Phase Separation and Magnetic Field Orientation. *Liq. Cryst.* **1994**, *16*, 127–134.

(120) Elices, M.; Llorca, J. *Fiber Fracture*; Elsevier Science Ltd: Kidlington, 2002.

(121) Frone, A. N.; Panaitescu, D. M.; Spataru, D. D.; Radovici, C.; Trusca, R.; Somoghi, R. *Preparation and Characterization of PVA Composites with Cellulose Nanofibers Obtained by Ultrasonication*; 2011; Vol. 6.

(122) Qua, E. H.; Hornsby, P. R.; Sharma, H. S. S.; Lyons, G.; McCall, R. D. Preparation and Characterization of Poly(Vinyl Alcohol) Nanocomposites Made from Cellulose Nanofibers. *J. Appl. Polym. Sci.* **2009**, *113* (4), 2238–2247.

(123) Liu, J. C.; Martin, D. J.; Moon, R. J.; Youngblood, J. P. Enhanced Thermal Stability of Biomedical Thermoplastic Polyurethane with the Addition of Cellulose Nanocrystals. *J. Appl. Polym. Sci.* **2015**, *132* (22), 1–8.

(124) Lu, J.; Wang, T.; Drzal, L. T. Preparation and Properties of Microfibrillated Cellulose Polyvinyl Alcohol Composite Materials. *Compos. Part A Appl. Sci. Manuf.* **2008**, *39* (5), 738–746.

(125) Jia, X.; Li, Y.; Cheng, Q.; Zhang, S.; Zhang, B. Preparation and Properties of Poly(Vinyl Alcohol)/Silica Nanocomposites Derived from Copolymerization of Vinyl Silica Nanoparticles and Vinyl Acetate. *Eur. Polym. J.* **2007**, *43* (4), 1123–1131.

(126) Sakuranda, I. *Polyvinyl Alcohol Fibers*; New York: M. Dekker, 1985.

(127) Jalal Uddin, A.; Araki, J.; Gotoh, Y. Toward "Strong" Green Nanocomposites: Polyvinyl Alcohol Reinforced with Extremely Oriented Cellulose Whiskers. *Biomacromolecules* **2011**, *12* (3), 617–624.

(128) Mariano, M.; Chirat, C.; El Kissi, N.; Dufresne, A. Impact of Cellulose Nanocrystal Aspect Ratio on Crystallization and Reinforcement of Poly(Butylene Adipate- Co - Terephthalate). *J. Polym. Sci. Part B Polym. Phys.* **2016**, *54* (22), 2284–2297.

(129) Frone, A. N.; Berlioz, S.; Chailan, J.-F.; Panaitescu, D. M. Morphology and Thermal Properties of PLA–cellulose Nanofibers Composites. *Carbohydr. Polym.* **2013**, *91* (1), 377–384.

(130) Lu, P.; Hsieh, Y. Lo. Preparation and Properties of Cellulose Nanocrystals: Rods, Spheres, and Network. *Carbohydr. Polym.* **2010**, *82* (2), 329–336.

(131) Mariano, M.; Chirat, C.; El Kissi, N.; Dufresne, A. Impact of Cellulose Nanocrystal Aspect Ratio on Crystallization and Reinforcement of Poly(Butylene Adipate-Co-Terephthalate). *J. Polym. Sci. Part B Polym. Phys.* **2016**, *54* (22), 2284–2297.

(132) Voronova, M. I.; Surov, O. V.; Guseinov, S. S.; Barannikov, V. P.; Zakharov, A. G. Thermal Stability of Polyvinyl Alcohol/Nanocrystalline Cellulose Composites. *Carbohydr. Polym.* **2015**, *130*, 440–447.

(133) Mariano, M.; Chirat, C.; El Kissi, N.; Dufresne, A. Impact of Cellulose Nanocrystal Aspect Ratio on Crystallization and Reinforcement of Poly(Butylene Adipate-Co-Terephthalate). *J. Polym. Sci. Part B Polym. Phys.* **2016**, *54*, 2284–2297.

(134) Lu, J.; Wang, T.; Drzal, L. T. Preparation and Properties of Microfibrillated Cellulose Polyvinyl Alcohol Composite Materials. *Compos. Part A Appl. Sci. Manuf.* **2008**, *39*, 738–746.

(135) Zhang, W.; He, X.; Li, C.; Zhang, X.; Lu, C.; Zhang, X.; Deng, Y. High Performance Poly (Vinyl Alcohol)/Cellulose Nanocrystals Nanocomposites Manufactured by Injection Molding. *Cellulose* **2014**, *21*, 485–494.

(136) Cheng, D.; Wen, Y.; An, X.; Zhu, X.; Ni, Y. TEMPO-Oxidized Cellulose Nanofibers (TOCNs) as a Green Reinforcement for Waterborne Polyurethane Coating (WPU) on Wood. *Carbohydr. Polym.* **2016**, *151*, 326–334.

(137) Endo, R.; Saito, T.; Isogai, A. TEMPO-Oxidized Cellulose Nanofibril/Poly(Vinyl Alcohol) Composite Drawn Fibers. *Polymer (Guildf).* **2013**, *54*, 935–941.

(138) Liu, D.; Li, J.; Sun, F.; Xiao, R.; Guo, Y.; Song, J. Liquid Crystal Microphase Separation of Cellulose Nanocrystals in Wet-Spun PVA Composite Fibers. *RSC Adv.* **2014**, *4*, 30784.

(139) Miao, X.; Tian, F.; Lin, J.; Li, H.; Li, X.; Bian, F.; Zhang, X. Tuning the Mechanical Properties of Cellulose Nanofibrils Reinforced Polyvinyl Alcohol Composites via Altering the Cellulose Polymorphs. *RSC Adv.* **2016**, *6*, 83356–

(140) Dhar, P.; Tarafder, D.; Kumar, A.; Katiyar, V. Effect of Cellulose Nanocrystal Polymorphs on Mechanical, Barrier and Thermal Properties of Poly(Lactic Acid) Based Bionanocomposites. *RSC Adv.* **2015**, *5*, 60426–60440.

(141) Orellana, J. L.; Wichhart, D.; Kitchens, C. L. Mechanical and Optical Properties of Polylactic Acid Films Containing Surfactant-Modified Cellulose Nanocrystals. *J. Nanomater.* **2018**, *2018*, 1–12.

(142) Qing, Y.; Cai, Z.; Wu, Y.; Yao, C.; Wu, Q.; Li, X. Facile Preparation of Optically Transparent and Hydrophobic Cellulose Nanofibril Composite Films. *Ind. Crops Prod.* **2015**, *77*, 13–20.

(143) Fu, T.; Montes, F.; Suraneni, P.; Youngblood, J.; Weiss, J. The Influence of Cellulose Nanocrystals on the Hydration and Flexural Strength of Portland Cement Pastes. *Polymers (Basel).* **2017**, *9* (9).

(144) Diaz, J. A.; Wu, X.; Martini, A.; Youngblood, J. P.; Moon, R. J. Thermal Expansion of Self-Organized and Shear-Oriented Cellulose Nanocrystal Films. *Biomacromolecules* **2013**, *14* (8), 2900–2908.

(145) Lee, K.-Y.; Aitomäki, Y.; Berglund, L. A.; Oksman, K.; Bismarck, A. On the Use of Nanocellulose as Reinforcement in Polymer Matrix Composites. *Compos. Sci. Technol.* **2014**, *105*, 15–27.

(146) Rol, F.; Belgacem, M. N.; Gandini, A.; Bras, J. Recent Advances in Surface-Modified Cellulose Nanofibrils. *Prog. Polym. Sci.* **2018**.

(147) Fujisawa, S.; Saito, T.; Kimura, S.; Iwata, T.; Isogai, A. Comparison of Mechanical Reinforcement Effects of Surface-Modified Cellulose Nanofibrils and Carbon Nanotubes in PLLA Composites. *Compos. Sci. Technol.* **2014**, *90*, 96–101.

(148) Lu, Y.; Cueva, M. C.; Lara-Curzio, E.; Ozcan, S. Improved Mechanical Properties of Polylactide Nanocomposites-Reinforced with Cellulose Nanofibrils through Interfacial Engineering via Amine-Functionalization. *Carbohydr. Polym.* **2015**, *131*, 208–217.

(149) Bello, S. A.; Agunsoye, J. O.; Hassan, S. B.; Zebase Kana, M. G.; Raheem, I. A. Tribology in Industry Epoxy Resin Based Composites, Mechanical and Tribological Properties: A Review. *Tribol. Ind.* **2015**, *37* (4), 500–524.

(150) Alamri, H.; Low, I. M.; Alothman, Z. Mechanical, Thermal and Microstructural Characteristics of Cellulose Fibre Reinforced Epoxy/Organoclay Nanocomposites. *Compos. Part B Eng.* **2012**, *43* (7), 2762–2771.

(151) Ansari, F.; Galland, S.; Johansson, M.; Plummer, C. J. G.; Berglund, L. A. Cellulose Nanofiber Network for Moisture Stable, Strong and Ductile Biocomposites and Increased Epoxy Curing Rate. *Compos. Part A Appl. Sci. Manuf.* **2014**, *63*, 35–44.

(152) Hu, Z.; Berry, R. M.; Pelton, R.; Cranston, E. D. One-Pot Water-Based Hydrophobic Surface Modification of Cellulose Nanocrystals Using Plant Polyphenols. *ACS Sustain. Chem. Eng.* **2017**, *5* (6), 5018–5026.

(153) Peng, S. X.; Moon, R. J.; Youngblood, J. P. Design and Characterization of Cellulose Nanocrystal-Enhanced Epoxy Hardeners. *Green Mater.* **2014**, *2*, 193–205.

(154) Peng, B. L.; Dhar, N.; Liu, H. L.; Tam, K. C. Chemistry and Applications of Nanocrystalline Cellulose and Its Derivatives: A Nanotechnology Perspective. *Can. J. Chem. Eng.* **2011**, *89* (5), 1191–1206.

(155) Yano, H.; Sugiyama, J.; Nakagaito, A. N.; Nogi, M.; Matsuura, T.; Hikita, M.; Handa, K. Optically Transparent Composites Reinforced with Networks of Bacterial Nanofibers. *Adv. Mater.* **2005**, *17* (2), 153–155.

(156) Asadi, A.; Miller, M.; Sultana, S.; Moon, R. J.; Kalaitzidou, K. Introducing Cellulose Nanocrystals in Sheet Molding Compounds (SMC). *Compos. Part A Appl. Sci. Manuf.* **2016**, *88*, 206–215.

(157) Lu, T.; Jiang, M.; Jiang, Z.; Hui, D.; Wang, Z.; Zhou, Z. Effect of Surface Modification of Bamboo Cellulose Fibers on Mechanical Properties of Cellulose/Epoxy Composites. *Compos. Part B Eng.* **2013**, *51*, 28–34.

(158) Barari, B.; Omrani, E.; Dorri Moghadam, A.; Menezes, P. L.; Pillai, K. M.; Rohatgi, P. K. Mechanical, Physical and Tribological Characterization of Nano-Cellulose Fibers Reinforced Bio-Epoxy Composites: An Attempt to Fabricate and Scale the 'Green' Composite. *Carbohydr. Polym.* **2016**, *147*, 282–293.

(159) Guhados, G.; Wan, W.; Hutter, J. L. Measurement of the Elastic Modulus of Single Bacterial Cellulose Fibers Using Atomic Force Microscopy. *Langmuir* **2005**, *21* (14), 6642–6646.

(160) Zhang, Y.; Song, P.; Liu, H.; Li, Q.; Fu, S. Morphology, Healing and Mechanical Performance of Nanofibrillated Cellulose Reinforced Poly(ε-Caprolactone)/Epoxy Composites. *Compos. Sci. Technol.* **2016**, *125*, 62–70.

(161) Lee, K.-Y.; Tammelin, T.; Schulfter, K.; Kiiskinen, H.; Samela, J.; Bismarck, A. High Performance Cellulose Nanocomposites: Comparing the Reinforcing Ability of Bacterial Cellulose and Nanofibrillated Cellulose. *ACS Appl. Mater. Interfaces* **2012**, *4* (8), 4078–4086.

(162) Xu, S.; Girouard, N.; Schueneman, G.; Shofner, M. L.; Meredith, J. C. Mechanical and Thermal Properties of Waterborne Epoxy Composites Containing Cellulose Nanocrystals. *Polym. (United Kingdom)* **2013**, *54* (24), 6589–6598.

VITA

Shikha Shrestha was born in Kathmandu, Nepal. She came to the United States to pursue undergraduate studies in 2010. She received a Bachelor of Science degree in Chemical Engineering from Worcester Polytechnic Institute (WPI), Worcester, MA, in 2014 and Ph.D. degree in Materials Engineering from Purdue University, West Lafayette, IN.